inorganics

MDPI

Article

Supramolecular Assemblies and Anticancer Activities of Aminopyidine-Based Polynuclear and Mononuclear Co(II) Benzoates: Experimental and Theoretical Studies

Kamal K. Dutta [1], Trishnajyoti Baishya [1], Rosa M. Gomila [2], Antonio Frontera [2,*], Miquel Barcelo-Oliver [2], Akalesh Kumar Verma [3], Jumi Das [3] and Manjit K. Bhattacharyya [1,*]

[1] Department of Chemistry, Cotton University, Guwahati 781001, Assam, India; chm2291001_kamal@cottonuniversity.ac.in (K.K.D.); baishyatrishnajyoti@gmail.com (T.B.)
[2] Departament de Química, Universitat de les Illes Balears, Crta de Valldemossa km 7.7, 07122 Palma de Mallorca, Baleares, Spain; rosa.gomila@uib.es (R.M.G.); miquel.barcelo@uib.es (M.B.-O.)
[3] Cell and Biochemical Technology Laboratory, Department of Zoology, Cotton University, Guwahati 781001, Assam, India; akhilesh@cottonuniversity.ac.in (A.K.V.); jumidas979@gmail.com (J.D.)
* Correspondence: toni.frontera@uib.es (A.F.); manjit.bhattacharyya@cottonuniversity.ac.in (M.K.B.)

Abstract: Two new Co(II) coordination compounds *viz.* $[Co(H_2O)(bz)_2(\mu\text{-}3\text{-}Ampy)_2]_n$ (**1**) and $[Co(4\text{-}Mebz)_2(2\text{-}Ampy)_2]$ (**2**) (wherebz = benzoate, 4-Mebz = 4-Methylbenzoate and Ampy = Aminopyridine) were synthesized and characterized via elemental (CHN), electronic spectroscopy, FT-IR spectroscopy, and thermogravimetric analysis (TGA). The molecular structures were determined by single-crystal X-ray diffraction analysis, inferring that compound **1** crystallizes as a *3-Ampy* bridged Co(II) coordination polymer, whereas compound **2** crystallizes as a mononuclear Co(II) compound. Compound **1** unfolds the presence of N–H···O, C–H···O, O–H···O, C–H···N and aromatic π···π interactions, while for compound **2**, N–H···O, C–H···O, C–H···C and C–H···π interactions are observed. Both the compounds showcase scarcely reported chelate ring interactions involving the benzoate moiety (chelate ring···π in **1** and N–H···chelate ring in **2**). We also conducted theoretical evaluations comprising of combined QTAIM/NCI plot analysis, DFT energy calculation and MEP surface analysis to analyze the supramolecular interactions present in the crystal structures. As per QTAIM parameters, the predominance of π-stacking interactions over hydrogen bonds in stabilizing the assembly in compound **1** is affirmed. Likewise, in compound **2**, both hydrogen bonding (HBs) and C–H···π interactions are deemed pivotal in stabilizing the dimeric assemblies. The in vitro antiproliferative activities of compounds **1** and **2** were performed against Dalton's lymphoma (DL) cancer cell lines through cytotoxicity and apoptosis assays, showcasing higher cytotoxicity of compound **1** (IC_{50} = 28 μM) over compound **2** (IC_{50} = 34 μM). Additionally, a molecular docking study investigated the structure–activity relationship of these compounds and allowed an understanding of the molecular behaviour after treatment.

Keywords: coordination polymer; DFT; QTAIM/NCI plot; apoptosis; cytotoxicity

check for updates

Academic Editor: Isabel Correia

Received: 23 December 2024
Revised: 29 January 2025
Accepted: 1 February 2025
Published: 10 February 2025

Citation: Dutta, K.K.; Baishya, T.; Gomila, R.M.; Frontera, A.; Barcelo-Oliver, M.; Verma, A.K.; Das, J.; Bhattacharyya, M.K. Supramolecular Assemblies and Anticancer Activities of Aminopyidine-Based Polynuclear and Mononuclear Co(II) Benzoates: Experimental and Theoretical Studies. *Inorganics* **2025**, *13*, 51. https://doi.org/10.3390/inorganics13020051

Correction Statement: This article has been republished with a minor change. The change does not affect the scientific content of the article and further details are available within the backmatter of the website version of this article.

Copyright: © 2025 by the authors. Licensee MDPI, Basel, Switzerland. This article is an open access article distributed under the terms and conditions of the Creative Commons Attribution (CC BY) license (https://creativecommons.org/licenses/by/4.0/).

1. Introduction

In recent years, there has been a significant surge in exploration into the design and fabrication of metal–organic compounds. This is primarily driven by their tuneable and functional properties, making them highly effective for a variety of applications [1–5]. Among those metal–organic compounds, coordination polymers stand out as structures formed through the combination of metal centres and various bridging ligands, offering a

fascinating array of network architectures and topologies [6]. Variable coordination modes of bridging organic ligands render them capable of constructing metalorganic compounds with tailored dimensionalities [7]. However, for achieving desired structural topologies in coordination compounds, the synthetic strategy requires careful manipulation of reaction parameters such as coordination geometry, pH, solvent temperature, etc., which influence the binding mode of the ligands, as well as the self-assemblies of the molecules [8,9].

For the synthesis of mononuclear and poly-nuclear coordination compounds, aromatic carboxylates are frequently employed as they possess desirable topologies from a crystal engineering perspective on account of their various coordination motifs, thermal endurance and capability to form bridging compounds with different metals [10,11]. Compounds that contain carboxylate synthons are excellent motifs for obtaining metal–organic hybrid assemblies and find applications in varying domains such as in biology etc. [12–14]. Specifically, both in vitro and in vivo anti-cancer studies have been performed for such systems with significant efficacy [15,16]. Aminopyridine ligands have also been used very extensively in the synthesis of compounds starting from simple mononuclear to polymeric coordination solids (CP's) holding different dimensionalities [17]. Another interesting feature possessed by these compounds is their desire to form different hydrogen bonds, like N–H···O between the amino NH and a coordinated carboxylate, which extends the structure from 1D to a 3D network [18]. Extra stability is also generated when π-stacking interactions are formed between the aromatic pyridyl ligands, playing a crucial role in stabilizing the supramolecular assemblies [19]. 3-Aminopyridine is a simple molecule of the aminopyridine series that can act both as a monodentate ligand via binding through the most basic *N*-pyridyl nitrogen, and a bridging ligand connecting two metal ions via the *N*-pyridyl and *N*-amino donor atoms [20,21]. 2-Aminopyridine is largely known for its diverse pharmacological importance, mostly for its usage in the synthesis of anti-inflammatoriesand antihistamines and the potential of its derivatives to coordinate with transition metals [22,23]. Several research groups have highlighted that metal carboxylates are of significant importance due to their potential biological activities [24–26]. Moreover, such complexes hold promise for various applications in catalysis, magnetism, optics, and related areas [27,28]. Pyridine-based coordination compounds also demonstrate substantial pharmaceutical potential *viz*. anti-inflammatory [29,30], antitumor [31,32], antimicrobial [33,34] and many others.

The most important criterion for supramolecular association is the non-covalent interactions, leading to a wide rangeof captivating network architectures and properties with befitting potential applications [35–37]. The investigation of non-covalent interactions in metal–organic compounds has received substantial attention, with a special focus on illuminating the mechanical properties and spatial organization of supramolecular assemblies [38]. Supramolecular self-assembly is an effective strategy for constructing metal–organic compounds and well-organized structures by employing various synthetic approaches and enabling the development of functional metal–organic compounds [39,40]. Among all types of non-covalent interactions, hydrogen bonding stands out as a powerful device in the creation of molecular solids due to its directional nature, selectivity, and reversible formation at ambient conditions [41]. Its contribution has been the key to the stabilization of supramolecular architectures [42]. Beyond the prominent hydrogen bonding networks exemplified by O–H···O and N–H···O, the subtle yet influential weak intermolecular C–H···N hydrogen bonding interactions significantly contribute to the stability of crystal structures [43–48]. Aromatic π-stacking interactions and interactions involving metal–ligand chelate ring(CR) also influence the supramolecular architectures in coordination compounds, thus emphasizing their vital significance not only in self-assembly but also in the investigation of the properties of functional materials [49–52]. In addition, the C–H···π interactions with aromatic π systems have been shown to play

significant roles in various fields of chemistry including crystal packing and biological systems [53].

In this study, we devoted our attention to supramolecular interactions in metal–organic compounds by reporting the synthetic method and crystal structures of two new Co(II) coordination compounds, *viz.* $[Co(H_2O)(bz)_2(\mu\text{-}3\text{-}Ampy)_2]_n$ (**1**) and $[Co(4\text{-}Mebz)_2(2\text{-}Ampy)_2]$ (**2**). Compound **1** crystallizes as a *3-Ampy* bridged Co(II) polymer, whereascompound **2** crystallizes as a mononuclear Co(II) compound. Additionally, the synthesized compounds were characterized by single-crystal XRD, elemental analysis, spectroscopic (FT-IR and electronic) techniques and TGA. Structural analysis of **1** and **2** reveals the presence of several non-covalent interactions which provide rigidity to the structures. Compound **1** reveals the presence of aromatic π stacking interactions along with some structure guiding H-bonding interactions ($R_2^2(8)$ synthon) and intramolecular CR$\cdots\pi$ interaction, whereas compound **2** unfolds the presence of N–H$\cdots$O, C–H$\cdots$O, C–H$\cdots$C, C–H$\cdots\pi$ and N–H$\cdots$CR interactions. We also carried out theoretical studies to analyze the non-covalent H-bonding, π-stacking and C–H$\cdots\pi$ interactions present in the crystal structures. We used DFT calculations, MEP surface analysis, NCI plot and QTAIM computational tools to explore the energetic features and the characteristics of the supramolecular assemblies. In this study, the in vitro antiproliferative activity of compounds **1** and **2** was evaluated against Dalton's lymphoma (DL) malignant cancer cell line. Cytotoxicity and apoptosis assays were used to assess the ability of these compounds to inhibit growth and induce cell death in DL cells. Additionally, molecular docking study was conducted to investigate the structure–activity relationship of these compounds. This combined approach aimed at a comprehensive evaluation of the potential of compounds **1** and **2** as anticancer agents and identified the key structural features responsible for their activity. Peripheral blood mononuclear cells (PBMC) were utilized to assess the potential cytotoxic effects of the tested compounds on normal, non-cancerous cells. Cisplatin, a well-known chemotherapeutic drug, was used as a reference standard in these experiments. By comparing the cytotoxic effects of the tested compounds to those of cisplatin, it is possible to benchmark their efficacy and safety.

2. Results and Discussion

2.1. Syntheses and General Aspects

Synthesis of $[Co(H_2O)(bz)_2(\mu\text{-}3\text{-}Ampy)_2]_n$ (**1**) was carried out by reacting two equivalents of sodium salt of benzoic acid, one equivalent of $CoCl_2{\cdot}6H_2O$ and two equivalents of *3-Ampy* at room temperature in aqueous medium. However, $[Co(4\text{-}Mebz)_2(2\text{-}Ampy)_2]$ (**2**) was produced by reacting one equivalent of $CoCl_2{\cdot}6H_2O$, two equivalents of the sodium salt of *4-Mebz* and two equivalents of *2-Ampy* at room temperature in aqueous medium. Both **1** and **2** are well dissolved in water and common organic media. Room temperature magnetic moment values are found to be 3.81 and 3.87 BM, respectively, for compounds **1** and **2**, corresponding to three unpaired electrons per Co(II) centre, which results from four oxygen weak field donors and two moderate N donor ligands [54–56].

2.2. Crystal Structure Analysis

The molecular structure of polymeric compound **1** is shown in Figure 1. Specific bond lengths along with the angles are presented in Table 1. The single-crystal X-ray diffraction study showcased that the compound crystallizes in a monoclinic crystal system with a $P2_1/c$ space group. In the crystal structure of compound **1**, there is a 1D polymeric chain that possesses Co(II) centres bridged by *3-Ampy* moieties. Moreover, one water molecule, two *bz* and other *3-Ampy* moieties are also bound to the metal centres. Thus, each Co(II) centre is hexa-coordinated with the O atom (O1W) from the water molecule,

carboxyl O atom (O10A) from the monodentate *bz*, carboxyl O atoms (O1A and O3A) from the bidentate *bz* and N1, N3 atoms from the two coordinated *3-Ampy* moieties. The coordination environment around each Co(II) centre is identified as a distorted octahedron, with O1W and N3 atoms in axial sites and O1A, O3A, O10A and N1 atoms occupying the equatorial sites. The distance between metal centres in compound **1** is found to be 6.05(4) Å. The average Co–O [2.1127(1) Å] and Co–N [2.1836(2) Å] bond lengths are comparable with the previous literature on Co(II) complexes [57].

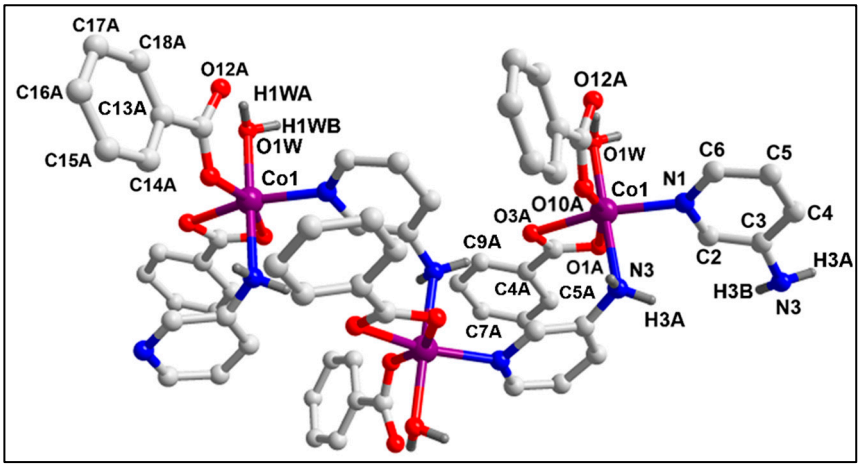

Figure 1. Solved crystal structure of $[Co(H_2O)(bz)_2(\mu\text{-}3\text{-}Ampy)_2]_n$ (**1**). The aromatic hydrogen atoms are omitted for clarity. Aromatic H's are numbered similarly to the carbon atom they are attached.

Table 1. Specific bond lengths (Å) and bond angles (°) of Co(II) centres in **1** and **2**, respectively.

Bond lengths and angles of **1** (Å, °)			
Co1–O1A	2.1414(12)	O10A–Co1–O1W	94.82(5)
Co1–O3A	2.1787(12)	O10A–Co1–N1	100.64(6)
Co1–O10A	2.0093(12)	O10A–Co1–N3	83.53(5)
Co1–O1W	2.1235(13)		
Co1–N1	2.0992(15)	O1W–Co1–O1A	91.95(5)
Co1–N3	2.2608(15)	O1W–Co1–O3A	88.64(5)
		O1W–Co1–N3	177.88(5)
O1A–Co1–O3A	60.88(5)		
O1A–Co1–N3	90.05(3)	N1–Co1–O1A	98.53(5)
		N1–Co1–O3A	159.38(6)
O3A–Co1–N3	92.96(5)	N1–Co1–O1W	93.47(5)
		N1–Co1–N3	85.53(6)
Bond lengths and angles of **2** (Å, °)			
Co1–O1	2.160(3)	O3–Co1–N3	107.77(13)
Co1–O4	2.328(3)	O3–Co1–N1	95.64(13)
Co1–O3	2.063(3)	N3–Co1–N1	100.36(14)
Co1–N1	2.099(3)	O3–Co1–O2	156.82(13)
Co1–N3	2.102(4)	N3–Co1–O2	90.82(13)
Co1–O2	2.160(3)	N1–Co1–O2	94.44(15)
O3–Co1–O1	96.69(12)	N1–Co1–O4	154.89(12)
N3–Co1–O1	145.05(14)	O2–Co1–O4	109.92(13)
N1–Co1–O1	101.69(13)	O1–Co1–O4	85.73(11)
O2–Co1–O1	60.78(12)		
O3–Co1–O4	59.48(11)		
N3–Co1–O4	85.69(13)		

The 1D polymeric chain of compound **1** is governed by non-covalent intra-molecular C–H···O, N–H···O, C–H···N hydrogen bonding interactions along with intramolecular non-covalent CR···π (CR = Chelate Ring) and C–H···C interactions (Figure 2). –C6H6 fragments of the bridging *3-Ampy* moieties are involved in C–H···O hydrogen bonding with the O12A atom from the monodentate *bz* moiety having C6–H6···O12A distance of 2.83(13) Å. Similarly, the –N3H3B fragments from the amino group of the *3-Ampy* ligand are engaged in N–H···O interactions with the O3A atom from the bidentate *bz* moieties with N3–H3A···O3A distance of 2.08(274) Å. C–H···N hydrogen bonding interactions are observed between the –C9AH9A fragments from the bidentate *bz* and N3 atom from the amino group of the *3-Ampy* moieties with C9A–H9A···N3 separation of 2.87(16) Å. Intramolecular CR···π interaction is observed between the bidentate Co-*bz* chelate and the π-system of *3-Ampy* moiety with centroid–centroid separation of 3.523(1) Å. Such kind of interaction involving metal-carboxylate (bidentate) chelate is very scarce in the literature. Additionally, C–H···C interactions are found between *bz* moieties from two adjacent monomeric units [C6A–H6A···C16A = 3.17(20) Å, C(sp^2)-C(sp^2), C6A···C16A= 3.96(32) Å; C14A–H14A···C8A = 3.30(19) Å; C(sp^2)-C(sp^2), C14A···C8A= 3.96(27) Å].

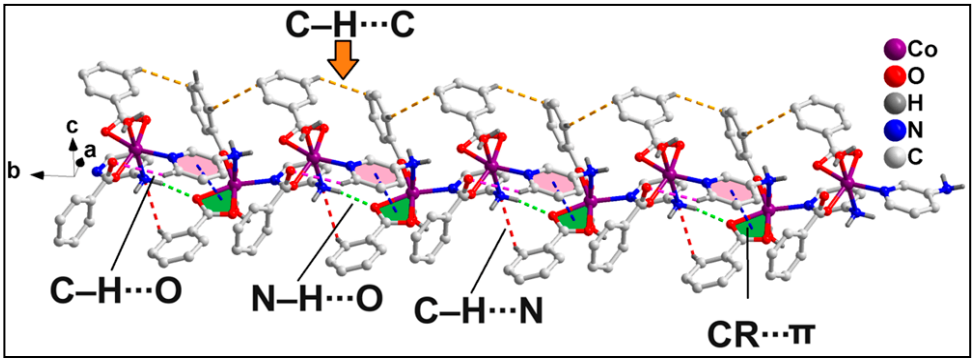

Figure 2. 1D polymeric chain of compound **1** involving intra-molecular CR···π, C–H···O, N–H···O, C–H···N and C–H···C interactions.

1D polymeric chains of compound **1** propagate along the crystallographic *ab* plane to form the layered architecture (Figure 3) of the compound which is stabilized by C–H···O hydrogen bonding and C–H···C interactions. The –C16AH16A fragments and carboxyl O12A atom of monodentate *bz* moieties from neighboring polymeric chains are involved in C–H···O hydrogen bonding with C16A–H16A···O12A separation of 2.56(13) Å. Moreover, the coordinated monodentate and bidentate *bz* moieties from adjacent polymeric chains also show the presence of C–H···C interactions [C17A–H17A···C7A = 3.22(22) Å, C(sp^2)-C(sp^2), C17A···C7A = 3.85(32) Å; C6A–H6A···C18A = 3.28(20) Å; C(sp^2)-C(sp^2), C6A···C17A = 3.68(30) Å].

The compound's 1D polymeric chains also propagate along the crystallographic *bc* plane to form the supramolecular layered assembly assisted by O–H···O and aromatic π-stacking interactions (Figure 4b). O1W atom of the coordinated water molecule and carboxyl O1A atom of bidentate *bz* moieties from two adjacent polymeric chains are engaged in O–H···O H-bonding with O1W–H1WB···O1A separation of 1.89(13) Å. This results in the generation of a $R_2^2(8)$ H-bonding synthon (Figure 4a), as denoted by Etter's graph set notation [58]. π-stacking interactions are found between the π-systems of *3-Ampy* and *bz* moieties from two adjacent polymeric chains with centroid (C4A-C9A)–centroid (C2-C6, N1) separation of 3.71(1) Å and slipped angle of 20.18° [59]. A dimeric segment of this assembly (Figure 4a) was theoretically analyzed *vide infra* (see Section 2.5).

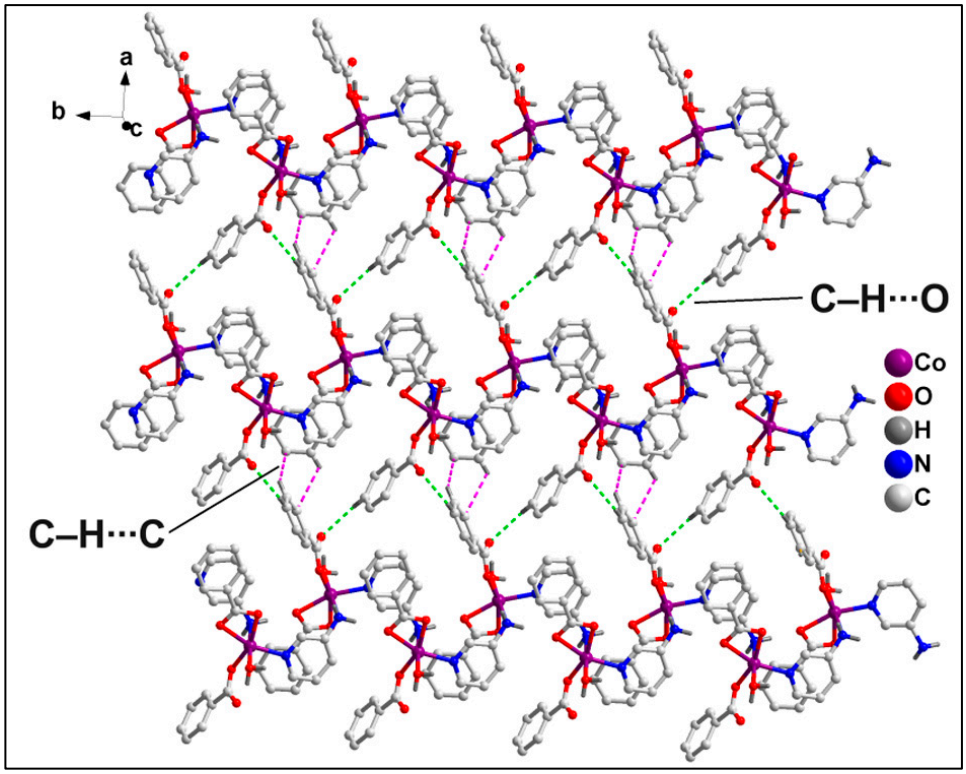

Figure 3. Layered assembly of polymeric complex **1** along the crystallographic *ab* plane assisted by C–H· · · O hydrogen bonding and C–H· · · C interactions.

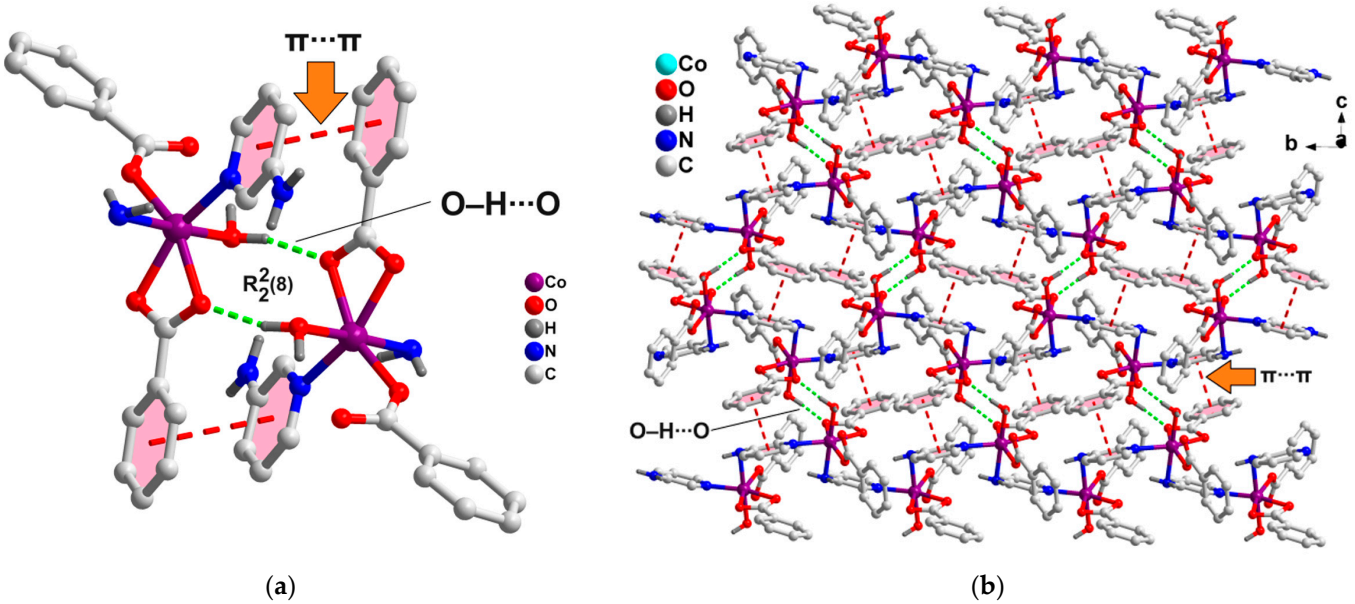

(**a**) (**b**)

Figure 4. (**a**) Supramolecular dimer showing $R_2^2(8)$ H-bonding synthon; (**b**) Layered architecture of compound 1 stabilized by O–H· · · O and aromatic π-stacking interactions along the crystallographic *bc* plane.

Figure 5 depicts the molecular structure of compound **2**. Specific bond lengths and bond angles are summarized in Table 1. The SCXRD analysis reveals that the compound crystallizes in a monoclinic crystal system with space group *Cc*. In the crystal structure of compound **2**, the Co(II) centre is hexacoordinated with four O atoms (O1, O2, O3 and O4) from two *4-Mebz* moieties and two N atoms (N1 and N3) from two *2-Ampy* moieties in a distorted octahedral geometry where the axial positions are occupied by O2 and O3

atoms, whereas the equatorial positions are occupied by O1, O4, N1 and N3 atoms. The Co(II) centre deviates by 0.5199 Å from the mean equatorial plane containing O1, O4, N1 and N3 atoms. The average Co–O [2.179(6) Å] and Co–N [2.096(6) Å] bond distances are almost consistent with the previously reported Co(II) complexes [60]. Some other research groups have also reported a number of closely related unique Co(II) complexes containing two *2-Ampy* ligands and two bidentate carboxylate moieties (not *4-Mebz*) [61–66]. Recently, our group has also reported a similar isomorphic compound of Zn(II) *viz.* $[Zn(4\text{-}MeBz)_2(2\text{-}AmPy)_2]$, only differing in the coordination geometry around Zn(II) and the binding mode of one *4-Mebz* moiety [67]. The coordination environment around the Zn(II) centre in that compound is penta-coordinated and the two *4-Mebz* ligands bind in both monodentate and bidentate fashion to the metal centre.

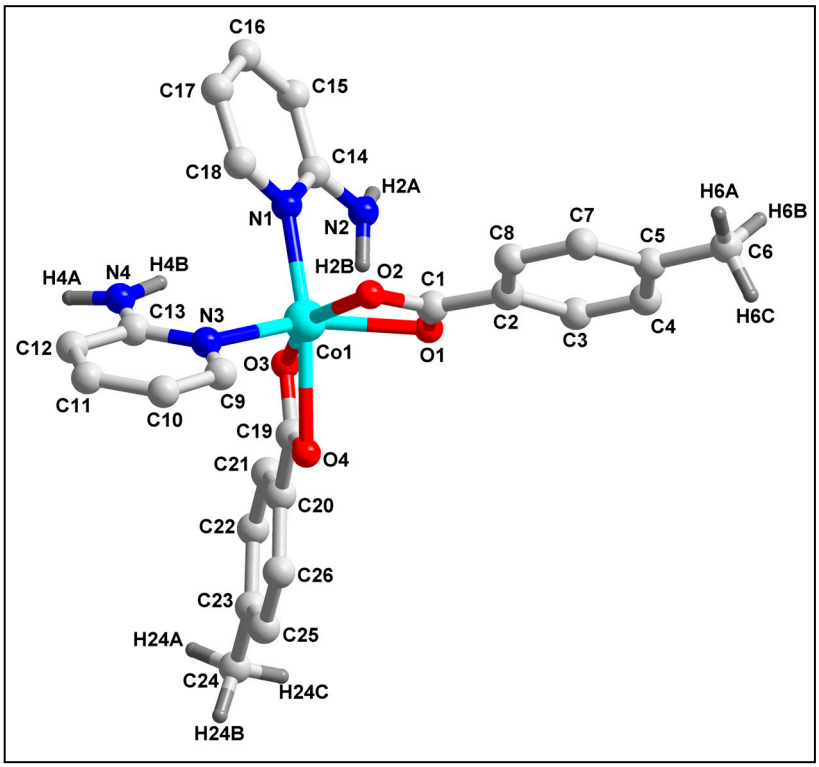

Figure 5. Molecular structure of $[Co(4\text{-}Mebz)_2(2\text{-}Ampy)_2]$ (**2**). The aromatic hydrogen atoms are omitted for clarity. Aromatic H's are numbered similarly to the carbon atom they are attached.

Adjacent monomeric units of the compound are interconnected via C–H···O hydrogen bonding, C–H···π and N–H···CR interactions, developing a 1D supramolecular chain, which grows along the crystallographic *c* axis (Figure 6). O4 carboxyl atom of *4-Mebz* is involved in C–H···O hydrogen bonding interaction with the –C12H12 moiety of *2-Ampy* of the neighbouring monomeric units with C12–H12···O4 separation of 2.58(6) Å. The –C4H4 and –C17H17 fragments from *4-Mebz* and *2-Ampy*, respectively, are involved in C–H···π interactions with the π-system of *4-Mebz* from neighbouring monomeric units with centroid(C20-C23, C25, C26)–H4 and centroid(C20-C23, C25, C26)–H17 distances of 2.79(1) and 2.60(1) Å, respectively. Unconventional N–H···CR interaction is found between the Co-*4-Mebz* chelate and the –N4H4B unit of *2-Ampy* moiety of the adjacent unit with N–H···CR distance of 3.00(1) Å.

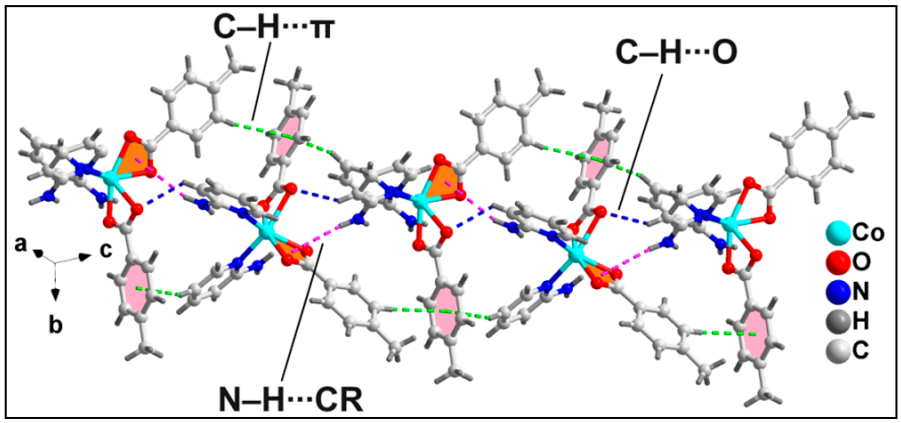

Figure 6. 1D supramolecular chain of compound **2** assisted by C–H· · · O and C–H· · · π interactions along the crystallographic *c* axis.

The supramolecular layers, extending along the *ac*-plane are formed through the linkage of adjacent 1D chains of compound **2** along the crystallographic *a*-axis via C–H· · · O hydrogen bonding and C–H· · · π interactions (Figure 7). C–H· · · O interactions are established between the –C24H24B fragment and O2 atom of *4-Mebz* from two neighboring monomeric complex units with C24–H24B· · · O2 distance of 2.64(7) Å. Moreover, the –C7H7 moiety of *4-Mebz* is involved in C–H· · · π interactions with the π-system of *2-Ampy* from two adjacent monomers with centroid(C14-C18, N1)–H7 separation of 2.73(1) Å.

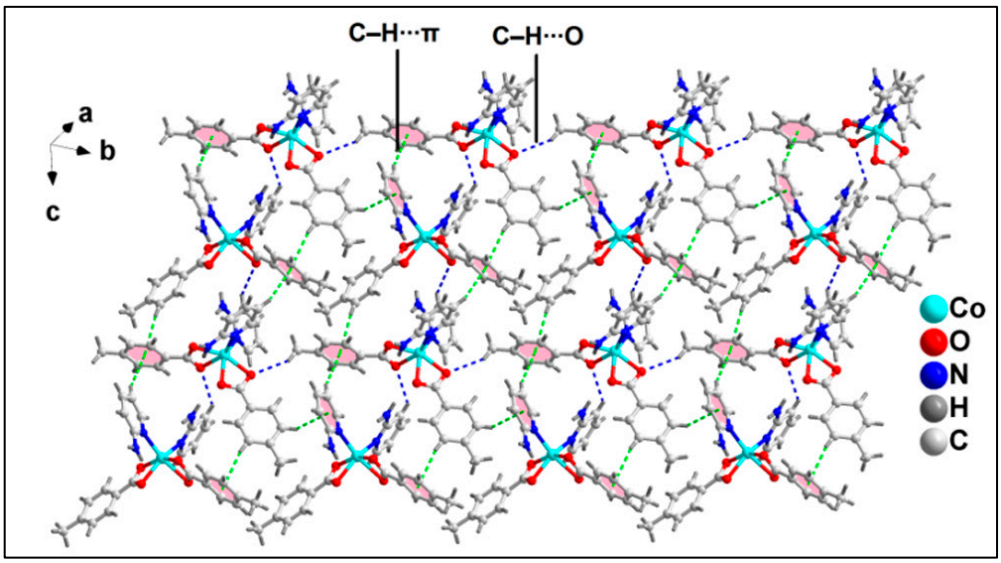

Figure 7. Layered architecture of compound **2** stabilized by C–H· · · O and C–H· · · π interactions along the crystallographic *ac* plane.

A closer look towards the crystal packing of compound **2** reveals the presence of an interesting dimeric fragment (Figure 8a) involving complex moieties and stabilized by C–H· · · O, N–H· · · O, C–H· · · C and C–H· · · π interactions. The C–H· · · O and N–H· · · O interactions result in the formation of a $R_2^2(8)$ H-bonding synthon, depicted by Etter's graph set notation [58]. C–H· · · O interactions are observed between the –C12H12 fragments of *2-Ampy* moieties and O4 atom of *4-Mebz* from two neighbouring mononuclear complex units with C12–H12· · · O4 distance of 2.58(6) Å (Table 2). Similarly, N–H· · · O hydrogen bonding interactions are observed between the –N4H4B fragments of *2-Ampy* and O1 atom of *4-Mebz* moieties from two adjacent monomers with N4–H4B· · · O1 distance of 2.09(6) Å. Again, the –C4H4 moiety of one *4-Mebz* is involved in C–H· · · π interactions with the

π-system of *4-Mebz* of the adjacent complex moiety in the dimer with centroid (C14-C18, N1)–H7 separation of 2.79(1) Å (corresponding C–H···π angle of 163.1°). The C–H···C interactions are observed between the *4-Mebz* moieties in the dimer [C6–H6C···C24 = 3.16 Å, C(sp^3)-C(sp^3), C6···C24= 3.83 Å; C6–H6B···C25 = 3.22(10) Å; C(sp^3)-C(sp^2), C6···C25 = 3.88(14) Å]. This dimeric fragment serves as a building block for the formation of another self-assembled layered structure aligned along the crystallographic *ab* plane (Figure 8b). This supramolecular dimer was established theoretically *vide infra* (Section 2.5).

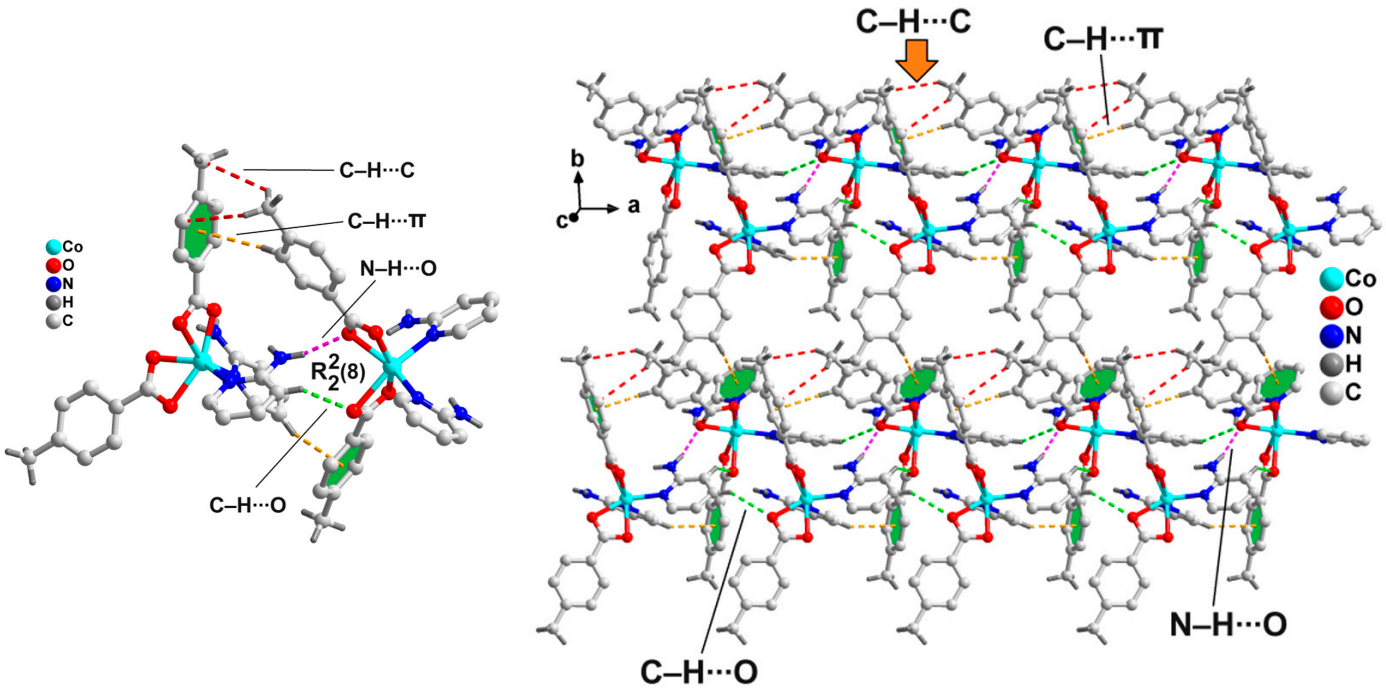

(**a**) (**b**)

Figure 8. (**a**) Supramolecular dimer of compound **2** stabilized by C–H···O, N–H···O, C–H···C and C–H···π interactions; (**b**) Layered assembly of compound **2** stabilized along the crystallographic *ab* plane.

Table 2. Selected hydrogen bond distances (Å) and angles (deg.) for compounds **1** and **2**.

D–H···A	d(D–H)	d(D···A)	d(H···A)	∠(DHA)
Compound **1**				
C6–H6···O12A	0.95	3.61	2.83	139.8
N3–H3A···O3A	0.89	2.96	2.08	169.6
C9–H9A···N3	0.95	3.43	2.87	119.1
C16A–H16A···O12A	0.95	3.42	2.56	151.8
O1W–H1WB···O1A	0.87	2.74	1.89	163.6
Compound **2**				
C12–H12···O4	0.95	3.26	2.58	129.2
C24–H24B···O2	0.98	3.48	2.64	144.2
N4–H4B···O1	0.88	2.95	2.09	164.0

2.3. Spectral Studies

2.3.1. FT-IR Spectroscopy

The FT-InfraRed spectra of the compoundsare performed in the frequency range of 4000–500 cm^{-1} (Figure S1). In the area of 3200–3600 cm^{-1} in the spectrum, the broad absorption peak indicates the O–H stretching vibration of the coordinated water molecule [68,69].

The spectrum also exhibits absorption bands corresponding to ρ_r (H_2O) (716 cm^{-1}) and ρ_w (H_2O) (685 cm^{-1}) supporting the presence of coordinated water molecules in **1** [70]. The difference in value between the asymmetric $\nu_{as}(COO^-)$ and symmetric $\nu_s(COO^-)$ stretching frequencies of the carboxylate moieties of compound **1** (204, 176 cm^{-1}) suggest unidentate [71] and chelate coordination modes of *bz* to the Co(II) centres in compound **1** [72]. However, the same for the carboxylate moiety [$\nu_{as}(COO^-)$-$\nu_s(COO^-)$] of **2** (191 cm^{-1}) indicates bidentate coordination of the *4-Mebz* ligands present in the compound [73]. The lack of bands near 1710 cm^{-1} in the spectra of both compounds confirms the deprotonation of the carboxyl groups of coordinated *bz* and *4-Mebz* moties [74]. In the spectra of both the compounds, the ring stretching modes of *3-Ampy* and *2-Ampy* ligands at 1601, 1507, 1435 and 1333 cm^{-1} have moved to higher wave numbers confirming the binding via the pyridine ring N atom to the metal centres [75]. The ring-wagging vibrations of pyridine groups are also obtained at around 655 and 716 cm^{-1} in both compounds [76,77]. The broad peak at 3423 cm^{-1} for compound **2** is attributed to the N–H stretching vibration of the coordinated *2-Ampy* molecule [62]. Moreover, $–NH_2$ stretching and bending vibrations of *3-Ampy* in compound **1** have moved to lower wave numbers, whereas $–NH_2$ wagging mode shifts to higher wave numbers supporting the binding of the amino group to the metal centres [62].

2.3.2. Electronic Spectroscopy

Both the solid and aqueous phase electronic spectra of **1** and **2** were determined and discussed in detail (Figures S2 and S3). The spectra of the compounds point to distorted octahedral geometry around the Co(II) centres in both **1** and **2**, respectively [48,75,78]. The $\pi \rightarrow \pi^*$ transition is observed due to the aromatic ligands and is assigned at the expected positions [79,80].

2.4. Thermogravimetric Analysis

Thermogravimetric analysis of the crystalline samples **1** and **2** was conducted between 25 and 800 °C under a dinitrogen atmosphere, following a heating rate of 10 °C/min (Figure S4). From the multistep weight loss process of compound **1**, it is assigned that the coordinated water molecules are lost first, followed by the loss of one of the coordinated *bz* moieties. A 34.57% (calcd: 33.66%) weight loss observed in the temperature range of 25−269 °C corresponds to the release of coordinated water molecules and one of the *bz* moieties [81]. The very next weight loss for **1** between 270 and 550 °C indicates the removal of the remaining benzoate moiety and *3-Ampy* moiety [82]. Compound 2 exhibits the first weight loss of 34.78% in the range 25–289 °C, corresponding to two *2-Ampy* ligands (calcd: 36.38%) [64]. The final weight loss of 51.23% between 290 and 567 °C corresponds to the removal of two *4-MeBz* moieties (calcd: 52.23%) [83].

2.5. Theoretical Study

The theoretical analysis is focused on examining the significant non-covalent interactions within both compounds that play a crucial role in determining their solid-state architecture. The theoretical study of compound **1** was directed towards the π-stacking and O–H···O hydrogen bonds as depicted in Figure 4a. These interactions are interchain and crucial for the development of the layered structure seen in compound **1** (Figure 4b). In the case of compound **2**, our investigation covers the hydrogen bonding and C–H···π interactions, which are pivotal in its X-ray crystal packing as evidenced in Figures 6–8. It is important to note that the polymeric chain of compound **1** propagates through Co–N coordination bonds linking the amino group of the *3-Ampy* ligand to the Co(II) metal centre. For our computational studies, a simplified monomeric model was employed, as shown in Figure 9, where the amino group in the apical position is substituted with NH_3. This

simplified model facilitates the examination of the interactions presented in Figure 4a. For this NH_3 group, the position of the N-atom was kept frozen and the H-atoms were optimized (for the cartesian coordinates in the ESI).

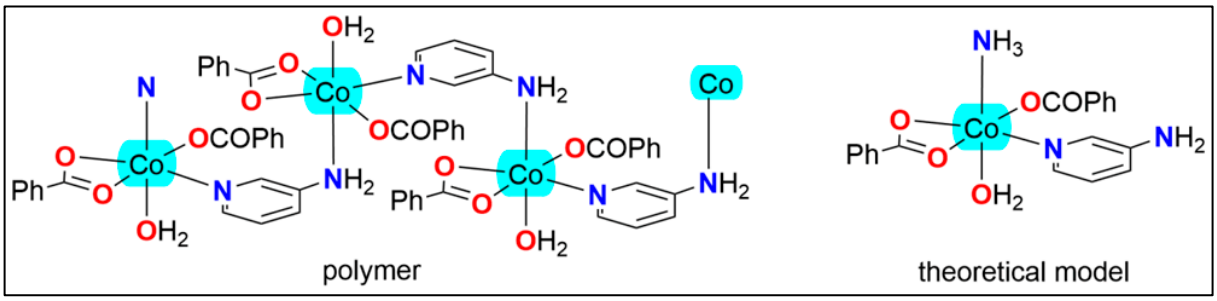

Figure 9. Chemical diagrams of the polymer (**left**) and the theoretical model (**right**) of **1**.

The theoretical investigation began by calculating the molecular electrostatic potential (MEP) surfaces for models of compounds **1** and **2** to identify their nucleophilic and electrophilic regions. For the model of compound **1**, as shown in Figure 10a, the MEP analysis reveals the MEP minimum near two oxygen atoms of the benzoate ligands at –50.8 kcal/mol, indicating a nucleophilic region. Additionally, a negative MEP value is observed at the oxygen atoms involved in the intramolecular hydrogen bond with the coordinated water molecule, registering at –42.7 kcal/mol. The MEP maximum, indicative of an electrophilic region, is found at the hydrogen atom of the coordinated water molecule not participating in the intramolecular hydrogen bond, with a value of 43.1 kcal/mol. The MEP is also significantly positive at the amino group of the *3-Ampy* ligand. Notably, the MEP shows a negative value over the centre of the benzoate's aromatic ring and a positive value over the *3-Ampy*'s centre, suggesting the propensity of these rings to engage in electrostatically enhanced π-stacking interactions. For compound **2**, as illustrated in Figure 10b, the MEP minimum is located at the oxygen atoms of the *4-Mebz* ligand, with a value of -55.0 kcal/mol, and the MEP maximum at the amino groups of *2-Ampy*, with a value of 46.1 kcal/mol. The MEP is negative over the centre of the *4-Mebz* aromatic ring, at -25.1 kcal/mol, and negligible over the centre of *2-Ampy*. Positive MEP values are observed at the aromatic hydrogen atoms of both *2-Ampy* and *4-Mebz*, at 23.2 kcal/mol and 9.4 kcal/mol, respectively, elucidating the role of C–H$\cdots\pi$ interactions in conjunction with hydrogen bonding between the amino and carboxylato groups in stabilizing the structure of compound **2**.

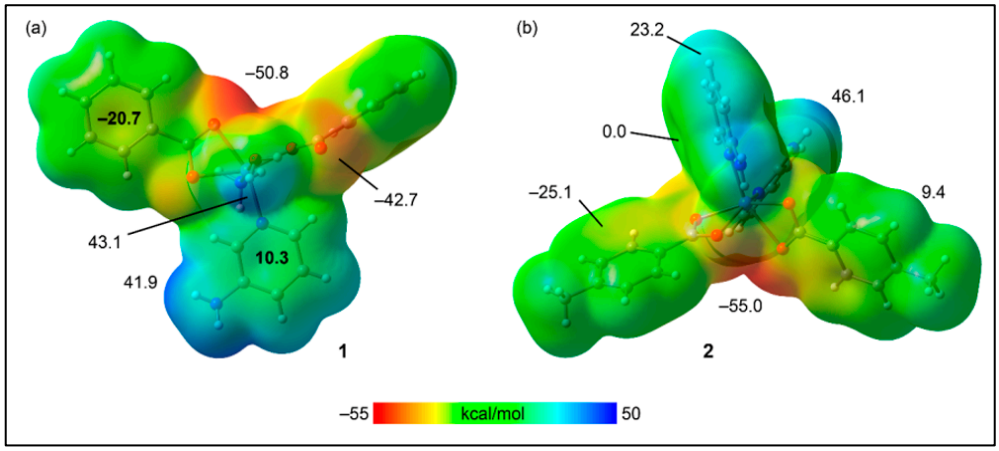

Figure 10. MEP surfaces of compounds **1** (**a**) and **2** (**b**). The MEP values at selected points of the surfaces are given in kcal/mol. Isovalue 0.001 a.u.

The QTAIM/NCI plot analysis of a self-assembled dimer of the model for compound **1** (Figure 4a), designed to replicate the interactions seen in the self-assembly of the 1D polymeric chains, is illustrated in Figure 11 (see Table S2 for QTAIM parameters). This analysis shows that each π-stacking interaction is characterized by two bond critical points (BCPs, depicted as small red spheres) and bond paths (represented by orange lines) that connect two carbon atoms from the benzoate and *3-Ampy* rings. The strong compatibility between the two rings is further underscored by a significant "reduced density gradient" (RDG) isosurface situated between them, corroborating the MEP surface analysis which indicated the strong ability to form π···π stacking due to the opposite electronic nature of the π-systems (one being electron-rich and the other electron-poor). Furthermore, the NCI plot analysis reveals two symmetrically equivalent BCPs and bond paths that characterize the O–H···O hydrogen bonds, each marked by blue RDG isosurfaces that signify the strength of these bonds. The robustness of these hydrogen bonds is verified by the QTAIM parameters, with a calculated strength of −14.8 kcal/mol. The total interaction energy, amounting to −35.4 kcal/mol, affirms the predominance of the π-stacking interactions, which are found to be even more significant than the hydrogen bonds in stabilizing the assembly.

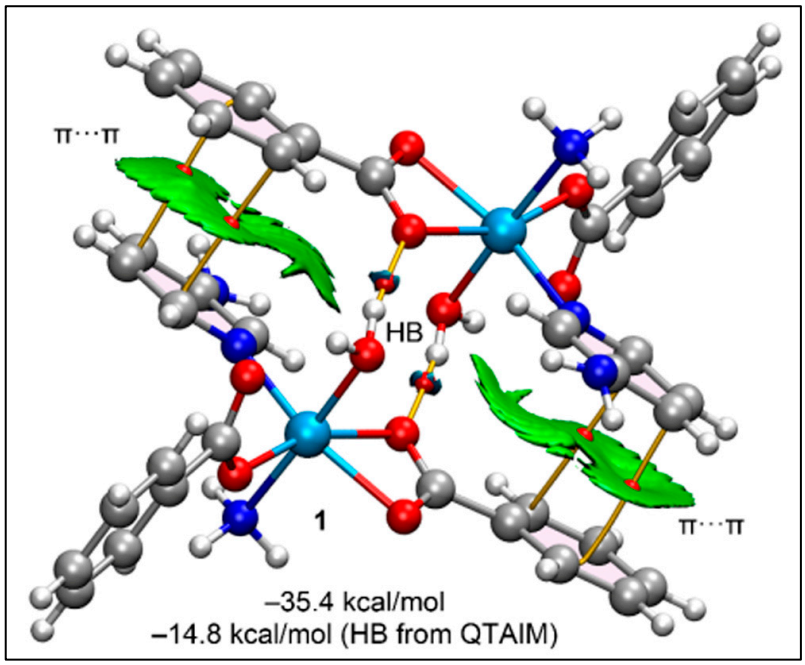

Figure 11. QTAIM (BCPs in red and bond paths as orange lines) and NCI plot of the dimeric assembly of compound **1** (RDG = 0.5, density cut-off = 0.04, colour range −0.04 a.u. ≤ (signλ_2)ρ ≤ 0.04 a.u. The dimerization energy is indicated. The contribution of the H-bonds was computed using the formula E = 0.5Vg, where V_g is the potential energy density.

Figure 12 illustrates the dimer of compound **2**, utilized to analyse and assess the N–H···O and C–H···π interactions highlighted in Figure 8a. The QTAIM analysis substantiates the presence of N–H···O, C–H···O, and C–H···π interactions through the identification of their respective bond critical points (BCPs) and bond paths (see Table S3 for QTAIM parameters). Specifically, the C–H···π interaction between the *2-Ampy* and the *4-Mebz* rings is marked by a unique BCP and a bond path that links the hydrogen atom of *2-Ampy* to a carbon atom of the *4-Mebz* ring. This C–H···π interaction is more distinctly visualized with the RDG surfaces, which encapsulate the entire π-system. Additionally, the interaction involving the *4-Mebz* ring showcases two BCPs and bond paths, incorporating the methyl group, with one BCP linking the hydrogen atom of one methyl group to the carbon atom of an adjacent methyl group, thus revealing the role of C–H···C(sp^3) interac-

tions alongside two C–H· · · C(sp^2) contacts. The total interaction energy of −20.8 kcal/mol underscores the significance of this dimer in the solid-state structure of compound **2**.

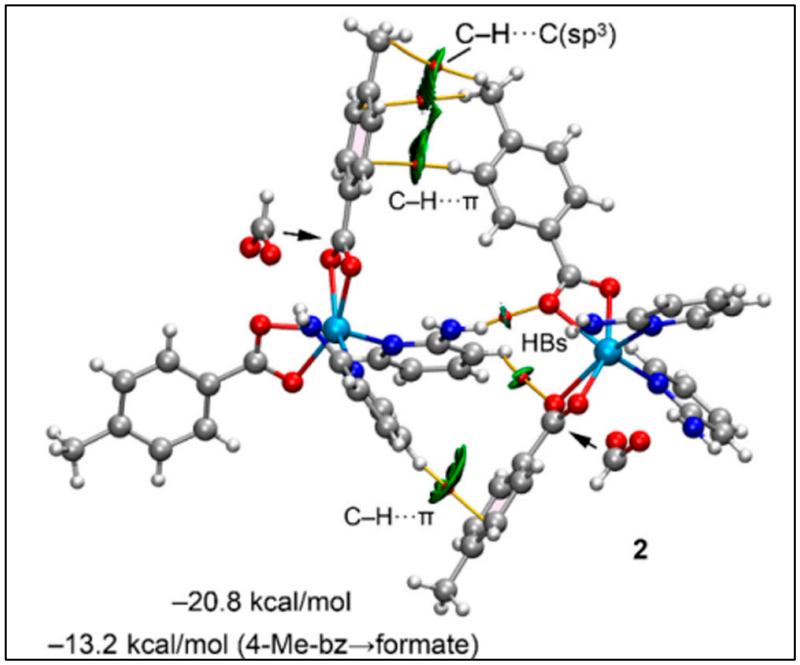

Figure 12. QTAIM (BCPs in red and bond paths as orange lines) and NCI plot of the dimeric assembly of compound **2** (RDG = 0.5, density cut-off = 0.04, colour range −0.04 a.u. ≤ (signλ_2)ρ ≤ 0.04 a.u. The dimerization energy for the complete assembly and the mutated one is indicated. For the mutated, model, the added H-atom of formate was optimized whilst the C and O-atoms were kept frozen.

To dissect the contribution of C–H· · · π interactions, a modified dimer was computed, wherein the *4-Mebz* ligands engaged in these interactions were substituted with formate ligands, thereby eliminating the C–H· · · π interactions. This alteration led to a reduced interaction energy of −13.2 kcal/mol, attributed to the hydrogen bonds. The difference with respect to the total interaction energy, amounting to −7.6 kcal/mol, is ascribed to the C–H· · · π interactions. Consequently, it is demonstrated that both hydrogen bonding (HBs) and C–H· · · π interactions are pivotal in stabilizing the dimeric assemblies. Thus, the theoretical study provides an interesting insight into the supramolecular dimers obtained in the crystal structure analysis of compounds **1** and **2**.

The interaction energies obtained for the dimers of **1** and **2** are comparable to those previously reported in similar systems, such as hydrogen bonds in metal complexes of dimethylaminopyridine [12] and Ni(II) coordination complexes of pyrazole [44]. Furthermore, CH· · · π and π· · · π interactions similar to those observed in this study were analyzed in Cu(II) complexes of 2,2′-bipyridine [48] and dimethylpyrazole [46].

2.6. Trypan Blue Assay

The Trypan Blue assay has remained an important method in anticancer research which evaluates cell viability by selectively staining the non-viable cells. Researchers employ this assay to evaluate the cytotoxicity of potential anticancer agents on cultured cells [84]. When cells undergo apoptosis upon treatment, their dead membranes allow Trypan Blue dye entry, staining them. Viable cells, with healthy membranes, forbiddye penetration. Calculation ofthe number of stained or non-viable cells provides useful insights into the effectiveness of anticancer treatments, facilitating the assessment of cell death induction and overall treatment impact [85]. In this cytotoxic study of both compounds, the Trypan Blue assay was employed to assess the number of viable cells in the DL cancer cells.

The findings demonstrated a significant dose-dependent increase in cytotoxicity/decrease in cell viability after a 48-h period (Figure 13a–c). From the viewpoint of the Trypan Blue cytotoxicity assay, these findings offer critical insights into the impact of specific treatments on cell morphology and integrity (Figure 13). The untreated control group (Figure 13a) exhibited typical morphology under microscopic examination, with cells appearing round and showing no apparent membrane abnormalities, establishing a baseline for comparison. On the other hand, noticeable changes were observed in the cellular morphology of the treated groups under high magnification. Dye staining disclosed two distinct alterations: chromatin condensation and membrane damage. The former one, characterized by the compacting of genetic material within the nucleus, is commonly associated with programmed cell death [86,87]. Membrane damage detection indicates structural deformation, likely induced by the cytotoxic impact of the treatment. The above evidence, based on the Trypan Blue assay, visually affirms the detrimental effects of the compounds under investigation.

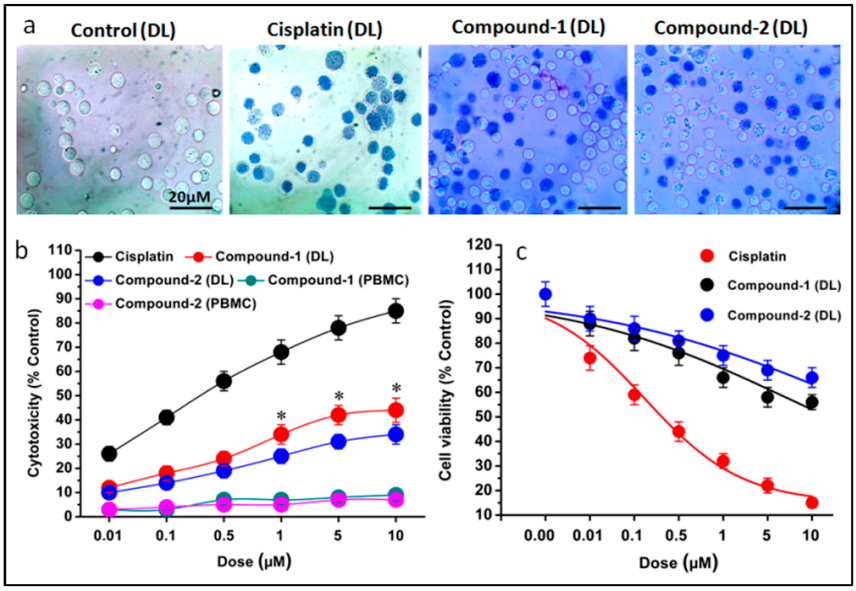

Figure 13. (**a**) Cytotoxic evaluation in DL cell line after 24-h treatment with varying concentrations of Compound **1** and Compound **2**. Dead cells are stained, while viable cells remain unstained. (**b**) Cell cytotoxicity (%) in normal (PBMC) and cancerous (DL) cells treated with different dosages of Compound **1** and Compound **2**. (**c**) Percentage of cell viability in DL cells following treatment with varying dosages of Compound **1** and Compound **2**. For positive control, cisplatin was considered. Data are mean ± S.D., n = 3, one-way ANOVA, * $p \leq 0.05$.

The half-maximal inhibitory concentration (IC_{50}) values signified the efficacy of the compounds in the DL cell line (Figure 14). The IC_{50} numbers for cisplatin, compound **1**, and compound **2** were found to be 0.51 μM, 28 μM, and 34 μM, respectively. This underscores the significant cytotoxic behaviour of the tested compounds, and further scope of their investigation as lead molecules in cancer treatment and research strategies. Comparative analysis showcases higher cytotoxicity of compound **1** over compound **2** in the DL cancer cell line. In contrast, minimal cytotoxicity (4–6%) was observed in the normal PBMC cell line treated with these compounds, with a statistically non-significant difference (Figure 13b). This selective cytotoxicity for the cancer cells while sparing the normal ones, represents a promising characteristic for potential therapeutic applications. Moreover, the free ligands (*bz* and *3-Ampy* for **1**, and *4-Mebz* and *2-Ampy* for **2**) associated with these compounds did not exhibit notable cytotoxic effects in the used cell line (Figure S5). This result describes

that the origin ofobserved cytotoxic effects lies in the complexes themselves rather than their individual ligands.

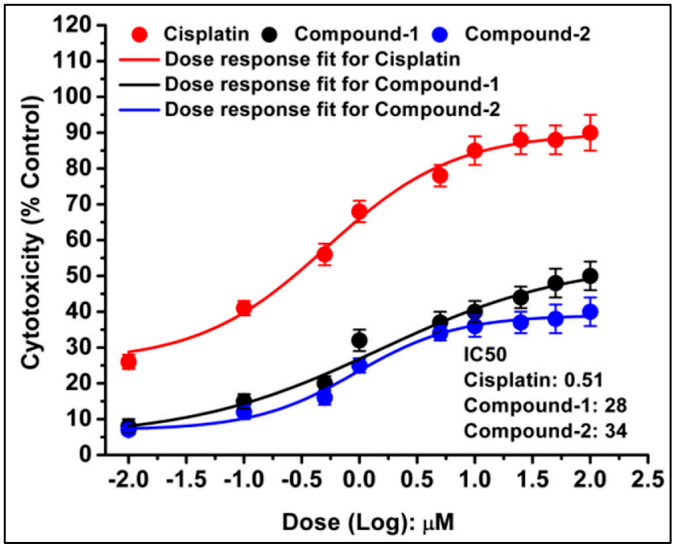

Figure 14. IC_{50} plot illustrating the efficacy of Compounds **1** and **2** in the DL cancer cell line, determined using a dose–response curve. The IC_{50} value represents the concentration of the compound required to inhibit cell viability by 50%, providing a measure of the compounds' cytotoxic potency. Data are mean ± S.D., n = 3.

2.7. Apoptosis Assay

To gain deeper insights into the cytotoxic mechanisms of the compounds, an apoptosis study was conducted. This investigation focuses on understanding the biological processes that regulate cell growth and proliferation. Apoptosis, characterized by changes in cell morphology such as increased membrane permeability to ethidium bromide resulting in red staining, contrasts with viable cells that appear green [88,89]. DL cells, on treatment with the synthesized compounds, showcased apoptotic features, including cell shrinkage, membrane blebbing, membrane fragmentation, and nuclear condensation (Figure 15). For reference purposes, the drug cisplatin is utilized because of its ability to exert cytotoxic effects by forming adducts with DNA, leading to DNA damageand ultimately inducing permanent apoptosis. DNA damage recognition proteins take part in transmitting signals of DNA damage to downstream signalling pathways involving p53, MAPK, and p73, which orchestrate the induction of apoptosis [90]. Moreover, there are reports indicating that most of the synthesized complexes had anticancer activity resulting from astable DNA adduct formation and apoptosis [91]. Again, cancer cells have a higher oxidative stress of cancer cells than normal cells which results in more oxidative DNA/protein damage [92]. Oxidative stress is a physiological condition characterized by elevated levels of reactive oxygen species (ROS) and free radicals. Various signalling pathways involved in carcinogenesis can influence ROS production and regulate downstream oxidative mechanisms, potentially impacting anticancer research [92]. In the comparative analysis of apoptotic cell death, compound **1** is found to induce greater cytotoxic effects and apoptosis than compound **2** after 48 h of exposure (Figure 15).

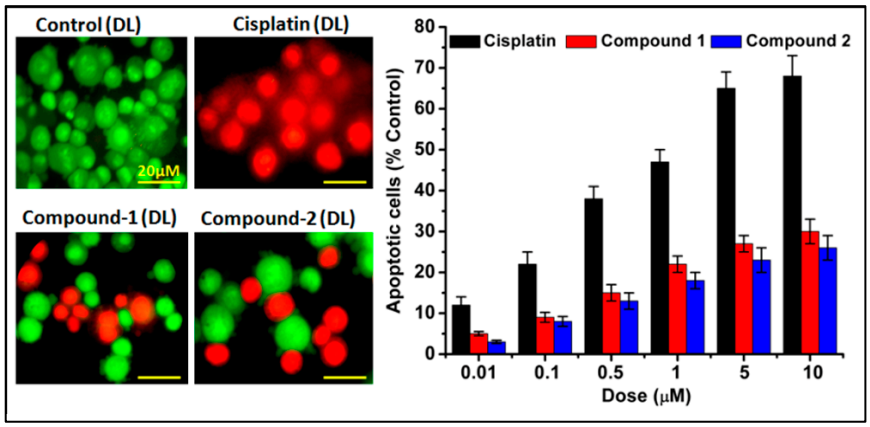

Figure 15. Fluorescence microscopy of DL cells showing distinct morphological features. Control cells display green nuclei, indicating viability. Cells treated with cisplatin (reference drug) exhibit red/orange nuclei, characteristic of apoptosis. Treatment with compound **1** and compound **2** results in apoptotic cells with visible membrane damage and blebbing. Apoptotic cells (in %) after treatment with compounds **1** and **2** showing dose-dependent increase in percent apoptotic cells. Data presented as mean ± S.D., n = 3.

2.8. Molecular Docking

Molecular docking has evolved as an effective drug design technique for determining the potency of drugs against specific target proteins [93]. It is possible to explore the binding affinities and interaction modes between compounds and the binding pocket of target proteins based on energy-based scoring functions [94]. It aids in rationalizing the biological results obtained and identifies the binding mode of the ligands with their receptors [95]. The target proteins BCL-2 and BCL-XL have crucial involvement in maintaining programmed cell death that are over-expressed in a variety of human cancers so targeting their evasion by their selective inhibition would offer effective therapeutic opportunities for cancer treatment [96]. Therefore, BCL-2 and BCL-XL were chosen as target proteins for docking with the synthetic compounds. The results exhibited significant docking scores which validated the findings of the biological activity of the compounds. The chemical interaction analysis suggested that the ligand–receptor complexes were effectively stabilized by specific hydrogen bonds and hydrophobic interactions (Table S1). Compound **1** was found to interact with active sites of amino acids such as Ala97 and Tyr199 of BCL-2 by three conventional H-bonds besides other hydrophobic and aromatic stacking interactions with the protein (Figure 16). It suggested that compound **1** revealed higher binding affinity as compared to the other compound due to the presence of extra H-bonds, as compound **2** has only one H-bond interaction with Arg104 (Figure 17). Compound **1** (Figure 18) showed two H-bonds with Lys20 and Ser145 of BCL-XL, whereas compound **2** interacted only with Lys20 of BCL-XL via one H-bond besides other interactions of different bond types (Figure 19). The results obtained from docking revealed that the synthetic compounds bind effectively with BCL-2 and BCL-XL where compound **1** excels over compound **2**. The above docking study was consistent with the findings obtained from the biological activity screening experiments including cell viability and apoptosis studies. The results of molecular docking, along with the evidence from the biological studies, indicate the potential BCL-2 and BCL-XL inhibitory roles of the compounds.

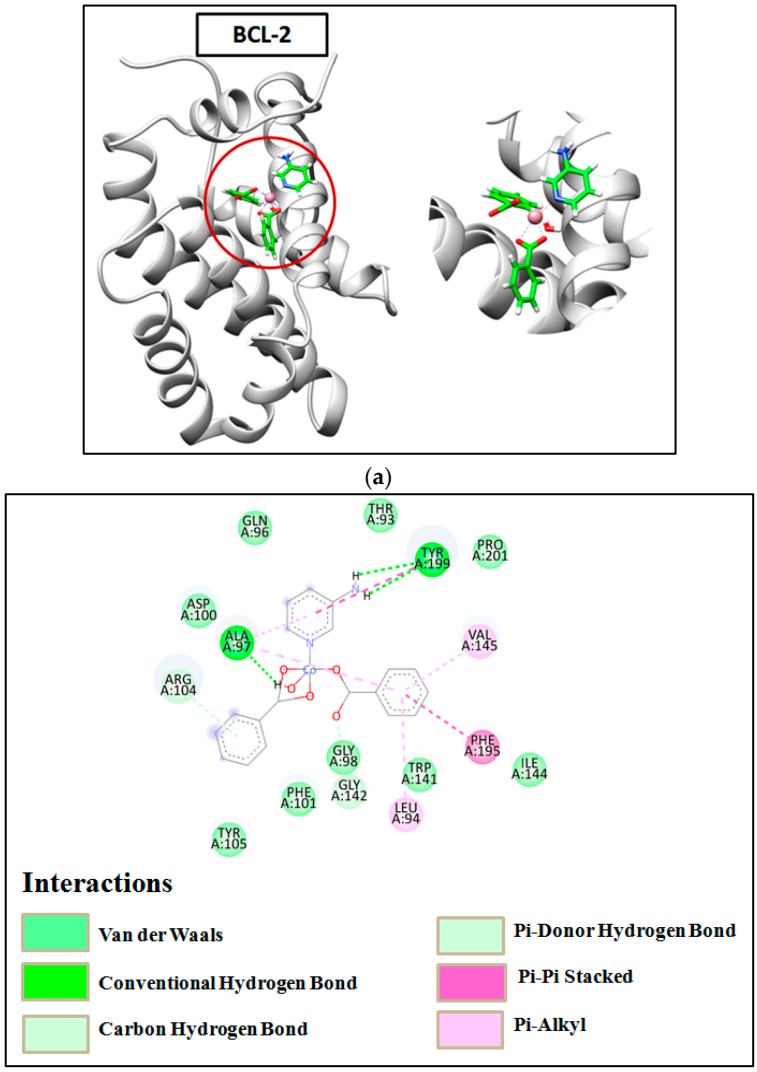

(**a**)

(**b**)

Figure 16. (**a**) Docking structure of compound **1** with the BCL-2 receptor, highlighting the interactions between the receptor and compound within the active sites; (**b**) Key binding interactions are depicted to provide insights into the molecular mechanism of action.

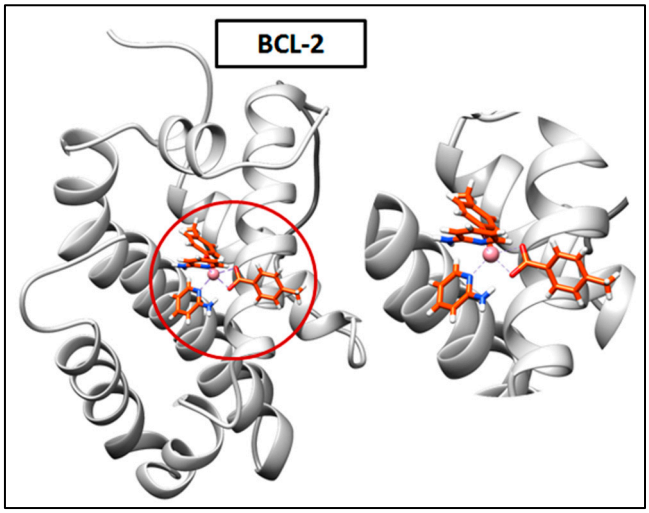

(**a**)

Figure 17. *Cont.*

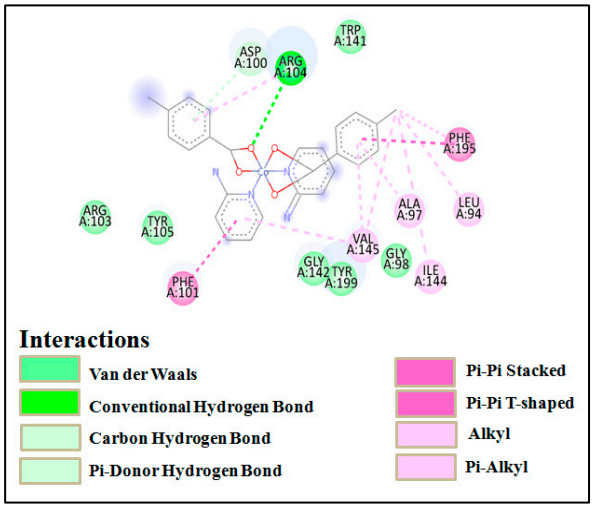

(**b**)

Figure 17. (**a**) Docking structure of compound **2** with the BCL-2 receptor, highlighting the interactions between the receptor and compound within the active sites; (**b**) Key binding interactions are depicted to provide insights into the molecular mechanism of action.

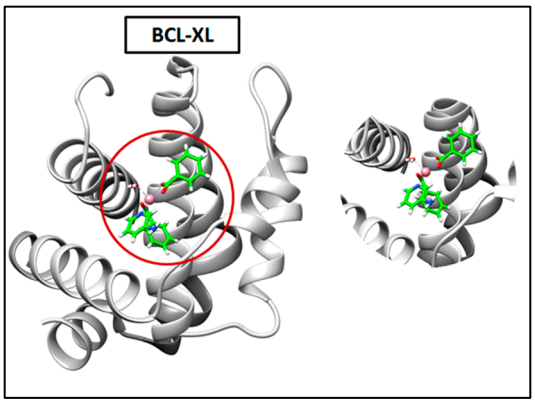

(**a**)

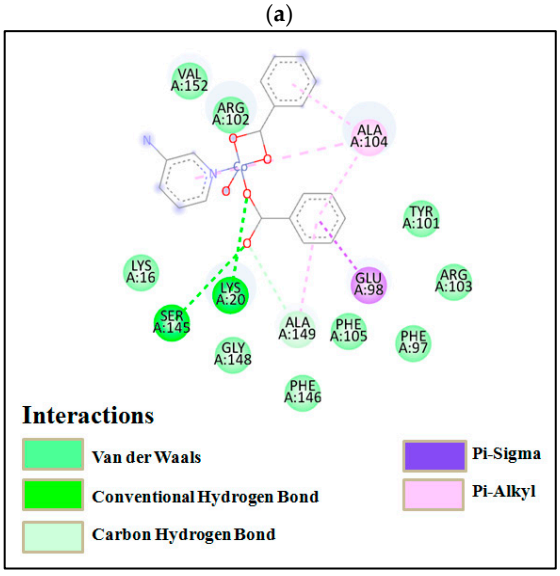

(**b**)

Figure 18. (**a**) Docking structure of compound **1** with the BCL-XL receptor, highlighting the interactions between the receptor and compound within the active sites; (**b**) Key binding interactions are depicted to provide insights into the molecular mechanism of action.

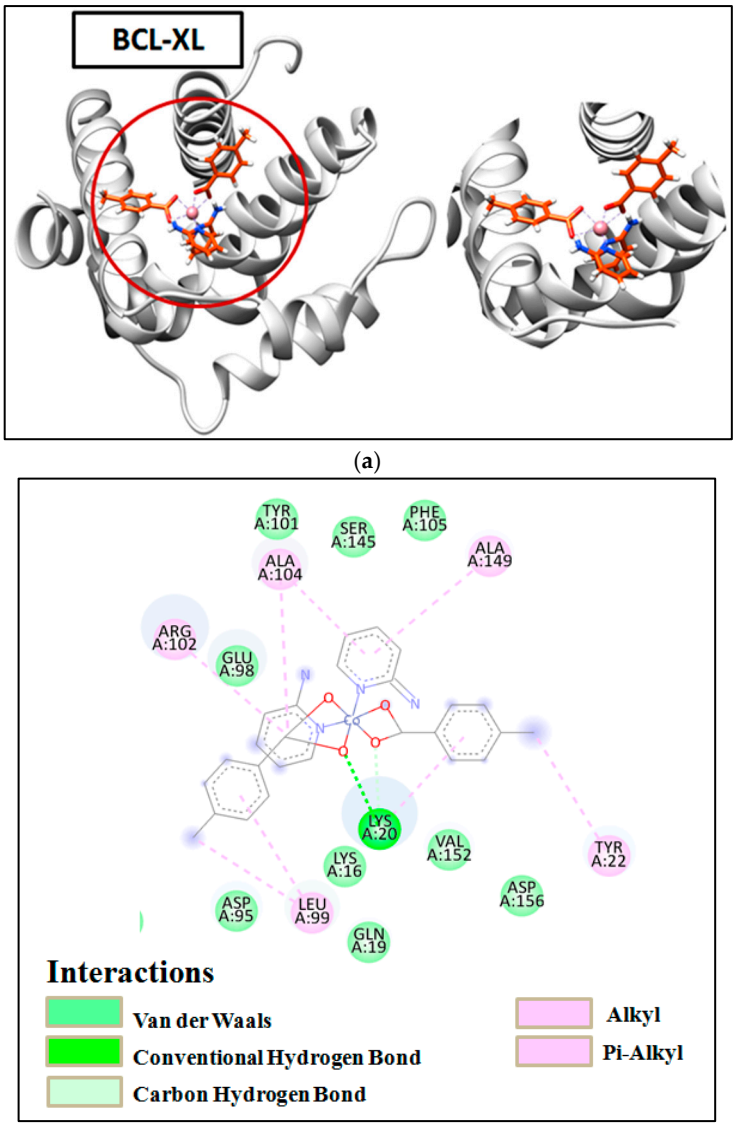

Figure 19. (**a**) Docking structure of compound **2** with the BCL-XL receptor, highlighting the interactions between the receptor and compound within the active sites; (**b**) Key binding interactions are depicted to provide insights into the molecular mechanism of action.

3. Materials and Methods

All the chemicals *viz.* cobalt(II) chloride hexahydrate, benzoic acid, 3-aminopyridine, 2-aminopyridine and 4-methyl benzoic acid that are readily available commercially (purchased from Sigma-Aldrich, India) are employed in the current research work. Perkin Elmer 2400 Series II CHN analyzer was used for elemental analysis (C, H, N). The FT-IR spectra from 500 to 4000 cm^{-1} were measured using KBr pellets with a Bruker Alpha Infrared spectrophotometer. Electronic spectra were recorded using a Shimadzu UV-2600 spectrophotometer. For solid-state spectra, $BaSO_4$ powder was used as a reference (100% reflectance). Thermogravimetric analysis was carried out from 25 to 800 °C (at a heating rate of 10 °C/min) under a dinitrogen atmosphere on a Mettler Toledo TGA/DSC1 STAR^e system. Room temperature magnetic moments of the synthesized compounds were calculated at 300 K using Sherwood Mark1 Magnetic Susceptibility balance by the Evans method.

3.1. Syntheses

3.1.1. Synthesis of $[Co(H_2O)(bz)_2(\mu\text{-}3\text{-}Ampy)_2]_n$ (**1**)

Compound **1** was prepared by dissolving 0.288g (2 mmol) of sodium salt of benzoic acid in 10 mL of distilled water, to which an aqueous solution (5 mL) of 0.237g (1 mmol) of $CoCl_2 \cdot 6H_2O$ was added with continuous stirring and then left at room temperature for an hour. To the resulting solution, an aqueous solution (5 mL) of 0.188g (2 mmol) of *3-Ampy* was added slowly and the mixture kept stirring for another hour (Scheme 1). The resulting pink solution was left undisturbed, and pink block-shaped single crystals were obtained after a few weeks by slow solvent evaporation in a refrigerator below 4 °C. Yield: 0.404 g (97.82%). Anal. calcd. For $C_{19}H_{18}CoN_2O_5$: C, 55.22%; H, 4.39%; N, 6.78%; Found: C, 54.87%; H, 4.23%; N, 6.50%. IR (KBr pellet, cm^{-1}): 3432 (br), 3348 (w), 3251 (sh), 2939 (w), 1899 (w), 1617 (sh), 1605 (s), 1539 (s), 1515 (sh), 1437 (sh), 1429 (s),1381 (s),1335 (w), 1265 (m), 1171 (w), 982 (m), 720 (sh), 716 (s), 685 (m), 655 (w), 640 (w), 552 (sh) (s, strong; m, medium; w, weak; br, broad; sh, shoulder).

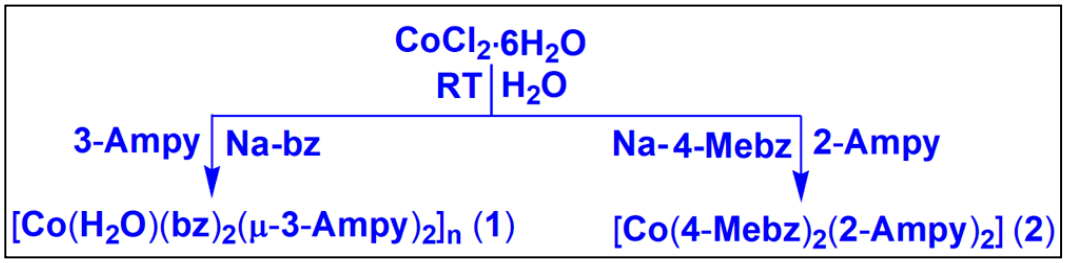

Scheme 1. Syntheses ofcompounds **1** and **2**.

3.1.2. Synthesis of $[Co(4\text{-}Mebz)_2(2\text{-}Ampy)_2]$ (**2**)

Compound **2** was prepared by dissolving 0.237g (1 mmol) of $CoCl_2 \cdot 6H_2O$ in 10 mL of distilled water, to which an aqueous solution (5 mL) of 0.300g (2mmol) of sodium salt of 4-methyl benzoic acid was added with continuous stirring and then left at room temperature for an hour. To the resulting solution, an aqueous solution (5 mL) of 0.188g (2 mmol) of *2-Ampy* was added slowly and the mixture kept stirring for another hour (Scheme 1). Under quiescent conditions, the resulting solution was allowed to undergo slow solvent evaporation in a refrigerator maintained below 4 °C, yielding light pink block-shaped single crystals after several weeks. Yield: 0.500 (96.71%). Anal. calcd. for $C_{26}H_{26}CoN_4O_4$: C, 60.35%; H, 5.06%; N, 10.83% Found: C, 60.30%; H, 5.00%; N, 10.79%; IR (KBr pellet, cm^{-1}): 3423 (br), 1914 (w), 1616 (sh), 1593 (s), 1514 (sh), 1437 (sh), 1399 (s), 1340 (w), 1225 (s), 1022 (s), 818 (m), 716 (m), 655 (w), 513 (m) (s, strong; m, medium; w, weak; br, broad; sh, Shoulder).

3.2. Crystallographic Data Collection and Refinement

D8 Venture diffractometer was used to determine the structures of compounds **1** and **2**, with a Photon III 14 detector, utilizing an Incoatec high brilliance IμS DIAMOND Cu tube equipped with an Incoatec Helios MX multilayer optics. Data reduction and cell refinements were performed using the Bruker APEX5 program [97]. SADABS is used for semi-empirical absorption correction, as well as scaling and merging the different datasets for the wavelength [97]. Crystal structures were solved by intrinsic phasing and refined with least squares minimization with SHELXL-2018/3 [98] using Olex2 software version 1.5 [99]. Refinement of all the non-hydrogen atoms was carried out with anisotropic thermal parameters by full-matrix least-squares calculations on F2. All hydrogen atoms, except those attached to O-atoms of water molecules and N-atoms of amine groups, were placed in ideal positions and refined in the isotropic approximation. Compound **2** was

found to be twinned (Twin law −1 0 0 0 −1 0 0 0 −1), with scales of 0.93(6) and 0.064(6). Diamond 3.2 software was used for drawing the figures [100]. Crystallographic data of compounds **1** and **2** are summarized in Table 3 with CCDC deposition numbers cited in Data Availability Statement.

Table 3. Crystallographic data and structure refinement details for **1** and **2**.

Parameters	**1**	**2**
Formula	$C_{19}H_{18}CoN_2O_5$	$C_{26}H_{26}CoN_4O_4$
Formula weight	413.28	517.44
Temp, [K]	100.0	100.0
Crystal system	Monoclinic	Monoclinic
Space group	$P2_1/c$	Cc
a, [Å]	13.5185(5)	9.8795(3)
b, [Å]	9.3996(4)	23.5377(8)
c, [Å]	14.2297(5)	10.5489(3)
α, [°]	90	90
β, [°]	91.846(2)	93.877(2)
γ, [°]	90	90
V, [Å^3]	1807.21(12)	2447.43(1)
Z	4	4
Absorption coefficient (mm^{-1})	7.744	5.829
F(0 0 0)	852.0	1076.0
ρ_{calc} g/cm^3	1.519	1.404
index ranges	$-16 \leq h \leq 16$, $-11 \leq k \leq 11$,	$-10 \leq h \leq 11$, $-28 \leq k \leq 28$,
	$-17 \leq l \leq 17$	$-12 \leq l \leq 12$
Crystal size, [mm^3]	0.13 × 0.12 × 0.08	0.21 × 0.14 × 0.12
2θ range, [°]	11.46 to 137.48	9.728 to 136.576
Independent Reflections	3297	3595
Reflections collected	31,819	28,791
Refinement method	Full-matrix	Full-matrix
	least-squares on F^2	least-squares on F^2
Data/restraints/parameters	3297/4/261	3595/6/335
Goodness-of-fit on F^2	1.073	1.035
Final R indices [I > 2σ(I)]	R_1 = 0.0317, wR_2 =0.0778	R_1 = 0.0384, wR_2 =0.0924
R indices (all data)	R_1 = 0.0327, wR_2 = 0.0790	R_1 = 0.0395, wR_2 = 0.0931
Largest hole and peak [e·Å^{-3}]	−0.55 and 0.358	−0.418 and 0.344

3.3. Computational Methods

The single-point calculations were carried out using the Turbomole 7.7 program [101] and the RI-BPE0 [102]/D4 [103]/def2-TZVP [104] level of theory. The crystallographic coordinates were used to evaluate the interactions in compounds **1** and **2** since we are interested in studying the noncovalent contacts as they stand in the solid state. High spin configuration was used for Co(II). Bader's "Atoms in molecules" theory (QTAIM) [105] and noncovalent interaction plot (NCI Plot) [106] were used to study the interactions discussed herein using the Multiwfn program [107] and represented using the VMD visualization

software [108]. For the calculation of the binding energies, we used the supramolecular approach, where the sum of the energies of the monomers was subtracted from the energy of the assembly. For the representation of the MEP surface, the 0.001 a.u. isosurface was used to emulate the van der Waals surface.

3.4. Cell Line and Drug Preparation

The anticancer potential of both the compounds was tested in Dalton's lymphoma (DL) malignant cell line (obtained by Professor Surya Bali Prasad from North Eastern Hill University, Shillong, India, in 2020). The DL cells were cultured in RPMI-1640 supplemented with 10% FBS, gentamycin (20 mg/mL^{-1}), streptomycin (100 mg/mL^{-1}) and penicillin (100 IU) in a CO_2 incubator at 37 °C with 5% CO_2; 80% confluent of exponentially growing cells were sub-cultured and used in the present study. The different doses (0.01, 0.1, 0.5, 1, 5 and 10 μM) of **1** and **2** were prepared by dissolving in conditioned media (pH = 7.4). PBMCs were used in the present study as healthy cells (non-cancerous) to check any toxic effect of synthesized complexes.

3.5. Trypan Blue Cytotoxicity Assay

In this assay, cells were stained with Trypan blue, a dye that selectively penetrates and colours non-viable cells (dead cells) with compromised cell membranes [109]. To assess the antiproliferative and cytotoxic potential of the cobalt complex and its associated ligand, a Trypan blue exclusion experiment was conducted using DL (cancer) and PBMC (normal) cell lines [110]. Following 48 h of in vitro treatment in appropriate culture media, cells were stained with trypan blue dye (4%) for 3 min. Subsequently, 1000 cells were counted across multiple fields of view for each experimental group (n = 3) to determine the percentage of cytotoxicity compared to the control.

The following is the non-linear curve fitting function used to obtain the IC_{50}:

$$y = \frac{(A2 - A1)}{\left(1 + 10^{((LOGx0 - x)p)}\right)}$$

where, $A1$ = bottom asymptote, $A2$ = top asymptote, $LOGx0$ = centre and p = hill slope.

Regarding the said free ligands, the observed cytotoxicity was found to be less than 6%, a value that did not reach statistical significance.

3.6. Apoptosis Study

Apoptotic cell death mediated by compounds **1** and **2** was assessed using the acridine orange/ethidium bromide (AO/EB) double staining method. AO is taken up by both viable and apoptotic cells, emitting green fluorescence under UV light, while EB is taken up only by apoptotic cells, emitting red fluorescence [111]. In this study, control and treated cancer cells were collected after 48 h of treatment, washed with PBS, and 20 μL of the AO/EB dye mixture (100 μg/mL of each dye in distilled water) was added to the cell suspension. The mixture was gently mixed and incubated in the dark for 5 min. The cells were then thoroughly examined under a fluorescence microscope and photographed. Approximately 1000 cells were analyzed, and the percentage of apoptotic nuclei was determined based on the differential staining pattern of the nuclei in three independent experiments. Viable cells exhibited bright, uniform green nuclei with organized structures, whereas apoptotic cells displayed condensed or fragmented chromatin with red or orange nuclei [112].

3.7. Molecular Docking Simulation

The results obtained from cell cytotoxicity and apoptosis studies were validated by carrying out molecular docking simulation using fully functional Molegro Virtual Docker

(Trial MVD 2010.4.0) software. Anti-apoptotic proteins considered for the study were BCL-2 (PDB: 2O22) and BCL-XL (PDB: 1R2D) and their crystal structures were downloaded from the Protein Data Bank. All co-factors and water molecules were removed before running the simulation program. MVD algorithm (MVD 2010 V-3) by default assigns charges to both receptors and ligands during the molecule preparation step. The docking settings used were a 15 Å radius grid, 0.30 in resolution with the number of runs: 10 runs; maximum interactions: 1500; maximum population size: 50; maximum steps: 300; neighbour distance factor: 1.00 and with a maximum of 5 poses returned. The best pose generated was visualized using Discovery Studio Visualization BIOVIA (version V4.5, 2024) and Chimera software (version V1.5, 2024).

3.8. Statistical Analysis

The experimental findings are showcased as mean ± S.D., n = 3 (all measurements performed thrice). An analysis of variance (ANOVA) (* $p \leq 0.05$) was used for data analysis, followed by post hocTukey's range test wherever necessary.

4. Conclusions

Two new Co(II) coordination compounds *viz.* polynuclear $[Co(H_2O)(bz)_2(\mu\text{-}3\text{-}Ampy)_2]_n$ (**1**) and mononuclear $[Co(4\text{-}Mebz)_2(2\text{-}Ampy)_2]$ (**2**) (where bz = benzoate, 4-Mebz = 4-methylbenzoate and Ampy = aminopyridine) were synthesized and characterized using single-crystal X-ray diffraction technique, FT-IR, electronic spectroscopy, TGA and elemental analyses. Crystal structure analysis of compound **1** reveals the presence of aromatic π-stacking and intramolecular chelate ring$\cdots\pi$ interactions in combination with several hydrogen bonding interactions, including a $R_2^2(8)$ synthon, which stabilizes the crystal structure. The layered assembly of compound **2** is stabilized by C–H$\cdots\pi$ interactions along with C–H$\cdots$O, N–H$\cdots$O hydrogen bonds forming another $R_2^2(8)$ Etter's ring. The studies on compounds **1** and **2** utilizing QTAIM/NCI plot and MEP analyses elucidated the importance of non-covalent interactions, such as π-stacking, hydrogen bonding (especially the $R_2^2(8)$ synthons) and C–H$\cdots\pi$ interactions that dictate their solid-state structures. For compound **1**, π-stacking and O–H$\cdots$O hydrogen bonds are key to its layered architecture, with MEP analysis highlighting the electronic complementarity between involved rings. In compound **2**, the balance of N–H$\cdots$O and C–H$\cdots\pi$ interactions, confirmed through QTAIM analysis and a strategic dimer modification, demonstrates that these interactions are important for the dimer's stability. Regarding their antiproliferative evaluation, present findings reveal that compound **1** demonstrated higher cytotoxicity with IC_{50}= 28μM and apoptosis-inducing potential compared to compound **2** (IC_{50}= 34μM) following a 48-h exposure period. Remarkably, negligible toxicity was observed in the normal PBMC cell line for both compounds. Further, the in silico docking study for compound **1** showed a higher number of interactions in comparison to compound **2** with both the BCL family proteins, which aligns well with the experimental findings. These results underscore the promising therapeutic potential of compound **1** in targeted cancer treatments, highlighting its efficacy in inducing cell death specifically in cancerous cells while sparing normal cells. Future studies could focus on elucidating the specific mechanisms underlying both the compounds selective cytotoxicity and further exploring their clinical applications in cancer therapy.

Supplementary Materials: The following supporting information can be downloaded at: https://www.mdpi.com/article/10.3390/inorganics13020051/s1, Figure S1: FT-IR spectra of compounds **1** and **2**; Figure S2: (a) UV-Vis-NIR spectrum of **1**, (b) UV-Vis spectrum of **1**; Figure S3: (a) UV-Vis-NIR spectrum of **2**, (b) UV-Vis spectrum of **2**; Figure S4: Thermogravimetric curves of compounds **1** and **2**; Figure S5: Cytotoxicity in DL cell line after 24-h treatment with 10 μM concentration of free ligands

associated with Compound **1** [(benzoate (bz) and 3-Aminopyridine(3-Ampy)] and Compound **2** [(4-Methylbenzoate (4-Mebz) and 2-Aminopyridine (2-Ampy)]. Dead cells are stained, while viable cells remain unstained. Table S1: Analysis of intermolecular interactions between antiapoptotic receptors and compounds **1** and **2**. The reference ligands, obtained from the co-crystallized PDB entry files of the respective receptors, were used for comparison. Binding score values are reported in arbitrary units, with lower scores indicating stronger affinity as calculated by the software algorithm; Table S2: QTAIM parameters (in a.u.) at the BCPs of the dimer of compound **1**; Table S3: QTAIM parameters (in a.u.) at the BCPs of the dimer of compound **2** Refs [48,75,78–80] were cited in Supplementary Materials.

Author Contributions: Conceptualization, A.F., A.K.V. and M.K.B.; methodology, A.F., A.K.V. and M.K.B.; software, A.F., R.M.G. and A.K.V.; formal analysis, A.F.; investigation, K.K.D.; T.B., J.D. and R.M.G.; data curation, M.B.-O.; writing—original draft preparation, K.K.D.; writing—review and editing, M.K.B.; visualization, A.F.; supervision, M.K.B.; project administration, A.F. and M.K.B.; funding acquisition, A.F. and M.K.B. All authors have read and agreed to the published version of the manuscript.

Funding: Financial supports obtained from SERB-SURE (Grant number: SUR/2022/001262), the In-House Research Project (IHRP), Cotton University [Grant number: CU/Dean/R&D/2019/02/23], ASTEC, DST, Govt. of Assam [Grant number: ASTEC/S&T/192(177)/2020-2021/43], and the Gobierno de Espana, MICIU/AEI (projects No. EQC2018-004265-P and PID2020-115637GB-I00) are gratefully acknowledged. K.K.D. thanks CSIR [09/1236(16497)/2023-EMR-I], Govt. of India for Junior Research Fellowship (JRF).The authors thank IIT, Guwahati for TG data.

Data Availability Statement: CCDC 2324863 and 2261047 contain the supplementary crystallographic data for Compounds **1** and **2**. These data can be obtained free of charge at http://www.ccdc.cam.ac.uk or from the Cambridge Crystallographic Data Centre, 12 Union Road, Cambridge CB2 1EZ, UK; fax: (+44) 1223-336-033; or E-mail: deposit@ccdc.cam.ac.uk.

Conflicts of Interest: The authors declare no conflicts of interest. The funders had no role in the design of the study; in the collection, analyses, or interpretation of data; in the writing of the manuscript; or in the decision to publish the results.

References

1. Climova, A.; Pivovarova, E.; Rogalewicz, B.; Raducka, A.; Szczesio, M.; Korona-Głowniak, I.; Korga-Plewko, A.; Iwan, M.; Gobis, K.; Czylkowska, A. New Coordination Compounds Based on a Pyrazine Derivative: Design, Characterization, and Biological Study. *Molecules* **2022**, *27*, 3467. [CrossRef]
2. Yang, D.-D.; Meng, F.-Q.; Shi, Y.-S.; Xiao, T.; Fang, Y.-H.; Tan, H.-W.; Zheng, X.-J. A Series of Zinc Coordination Compounds Showing Persistent Luminescence and Reversible Photochromic Properties via Charge Transfer. *Chem. Eng. J.* **2023**, *466*, 143202. [CrossRef]
3. Pellei, M.; Del Bello, F.; Porchia, M.; Santini, C. Zinc Coordination Complexes as Anticancer Agents. *Coord. Chem. Rev.* **2021**, *445*, 214088. [CrossRef]
4. Gul, Z.; Khan, S.; Ullah, S.; Ullah, H.; Khan, M.U.; Ullah, M.; Altaf, A.A. Recent Development in Coordination Compounds as a Sensor for Cyanide Ions in Biological and Environmental Segments. *Crit. Rev. Anal. Chem.* **2024**, *54*, 508. [CrossRef]
5. Yıldırım, A.; Aksoy, M.S. Homoleptic Pyrazinoic Acid Transition Metal Complex as an Efficient Catalyst toward Elegant Three-Component Synthesis of 3,4-Dihydro-2H-1,3-Benzoxazines. *Inorg. Chim. Acta* **2023**, *555*, 121583. [CrossRef]
6. Uvarova, M.A.; Lutsenko, I.A.; Babeshkin, K.A.; Sokolov, A.V.; Alexandrov, E.V.; Efimov, N.N.; Shmelev, M.A.; Khoroshilov, A.V.; Eremenko, I.L.; Kiskin, M.A. Solvent Effect in the Chemical Design of Coordination Polymers of Various Topologies with Co^{2+} and Ni^{2+} Ions and 2-Furoate Anions. *CrystEngComm* **2023**, *25*, 6786. [CrossRef]
7. Kateshali, K.; Farahmand, A.; Gholizadeh Dogaheh, S.; Soleimannejad, J.; Blake, A.J. Structural Diversity and Applications of Ce(III)-Based Coordination Polymers. *Coord. Chem. Rev.* **2020**, *419*, 213392. [CrossRef]
8. Amani, V.; Esmaeili, M.; Norouzi, F.; Khavasi, H.R. A Strategy for Obtaining Isostructurality Despite Structural Diversity in Coordination Compounds. *CrystEngComm* **2024**, *26*, 543. [CrossRef]
9. Ma, C.-Y.; Li, X.-X.; Du, M.-X.; Dong, W.-K.; Ding, Y.-J. Deep Insights into Novel Hexa-Coordinated Phenoxy-Bridged Trinuclear Ni(II) Asymmetric Salamo-like Complexes Affected by Different Types of Combined Solvents. *J. Mol. Struct.* **2024**, *1298*, 137071. [CrossRef]

10. Danilescu, O.; Bulhac, I.; Shova, S.; Novitchi, G.; Bourosh, P. Coordination Compounds of Copper(II) with Schiff Bases Based on Aromatic Carbonyl Compounds and Hydrazides of Carboxylic Acids: Synthesis, Structures, and Properties. *Russ. J. Coord. Chem.* **2020**, *46*, 838. [CrossRef]
11. Gu, J.; Wan, S.; Kirillova, M.V.; Kirillov, A.M. H-Bonded and Metal(II)–Organic Architectures Assembled from an Unexplored Aromatic Tricarboxylic Acid: Structural Variety and Functional Properties. *Dalton Trans.* **2020**, *49*, 7197. [CrossRef]
12. Boruah, R.; Bhattacharjee, S.; Dutta Purkayastha, R.N.; Modak, S.; Aktar, T.; Maiti, D.; Sieroń, L.; Maniukiewicz, W.; Gomila, R.M.; Frontera, A. Insights into Synthesis, Crystal Structure, Bioactivity and Computational Studies of Cu(II) and Zn(II) Carboxylates Containing Aminopyridine. *ChemistrySelect* **2023**, *8*, e202204937. [CrossRef]
13. Uddin, N.; Rashid, F.; Haider, A.; Tirmizi, S.A.; Raheel, A.; Imran, M.; Zaib, S.; Diaconescu, P.L.; Iqbal, J.; Ali, S. Triorganotin(IV) Carboxylates as Potential Anticancer Agents: Their Synthesis, Physiochemical Characterization, and Cytotoxic Activity against HeLa and MCF-7 Cancer Cells. *Appl. Organomet. Chem.* **2021**, *35*, e6165. [CrossRef]
14. Abdolmaleki, S.; Ghadermazi, M.; Aliabadi, A. Study on Electrochemical Behavior and In Vitro Anticancer Effect of Co(II) and Zn(II) Complexes Containing Pyridine-2,6-Dicarboxylate. *Inorg. Chim. Acta* **2021**, *527*, 120549. [CrossRef]
15. Štarha, P.; Křikavová, R. Platinum(IV) and Platinum(II) Anticancer Complexes with Biologically Active Releasable Ligands. *Coord. Chem. Rev.* **2024**, *501*, 215578. [CrossRef]
16. Alhoshani, A.; Sulaiman, A.A.; Sobeai, H.M.A.; Qamar, W.; Alotaibi, M.; Alhazzani, K.; Monim-ul-Mehboob, M.; Ahmad, S.; Isab, A.A. Anticancer Activity and Apoptosis Induction of Gold(III) Complexes Containing 2,2′-Bipyridine-3,3′-Dicarboxylic Acid and Dithiocarbamates. *Molecules* **2021**, *26*, 3973. [CrossRef] [PubMed]
17. Mautner, F.A.; Jantscher, P.V.; Fischer, R.C.; Torvisco, A.; Reichmann, K.; Massoud, S.S. Syntheses, Structural Characterization, and Thermal Behaviour of Metal Complexes with 3-Aminopyridine as Co-Ligands. *Transit. Met. Chem.* **2021**, *46*, 191. [CrossRef]
18. Yurtcan, S.; Yolcu, Z. 4-Aminopyridine Containing Metal-2,6-Pyridine Dicarboxylates and Complex Embedded Hydrogels: Synthesis, Characterization and Antimicrobial Applications. *Inorg. Chim. Acta* **2024**, *563*, 121918. [CrossRef]
19. Mautner, F.A.; Jantscher, P.; Fischer, R.C.; Torvisco, A.; Vicente, R.; Karsili, T.N.V.; Massoud, S.S. Synthesis and Characterization of 1D Coordination Polymers of Metal(II)-Dicyanamido Complexes. *Polyhedron* **2019**, *166*, 36. [CrossRef]
20. Yufanyi, D.M.; Nono, H.J.; Yuoh, A.C.B.; Tabong, C.D.; Judith, W.; Ondoh, A.M. Crystal Packing Studies, Thermal Properties, and Hirshfeld Surface Analysis in the Zn(II) Complex of 3-Aminopyridine with Thiocyanate as Co-Ligand. *Open J. Inorg. Chem.* **2021**, *11*, 63. [CrossRef]
21. Kartal, Z.; Şahin, O.; Yavuz, A. The Synthesis of Two New Hofmann-Type M(3-Aminopyridine)$_2$Ni(CN)$_4$ [M = Zn(II) and Cd(II)] Complexes and the Characterization of Their Crystal Structure by Various Spectroscopic Methods. *J. Mol. Struct.* **2018**, *1171*, 578. [CrossRef]
22. Beddar, K.; Bouchoucha, A.; Bourouai, M.A.; Zaater, S.; Djebbar, S. Transition Metal Complexes of 2-Aminopyridine Derivatives as Cyclooxygenase Inhibitors: Stability, Spectral, and Thermal Characterization, Electrochemical Behavior, DFT Calculations, Molecular Docking, and Biological Activities. *Russ. J. Gen. Chem.* **2023**, *93*, 2578. [CrossRef]
23. Mahmoud, W.H.; Mohamed, G.G.; El-Dessouky, M.M.I. Synthesis, Structural Characterization, In Vitro Antimicrobial and Anticancer Activity Studies of Ternary Metal Complexes Containing Glycine Amino Acid and the Anti-Inflammatory Drug Lornoxicam. *J. Mol. Struct.* **2015**, *1082*, 12. [CrossRef]
24. Studer, V.; Anghel, N.; Desiatkina, O.; Felder, T.; Boubaker, G.; Amdouni, Y.; Ramseier, J.; Hungerbühler, M.; Kempf, C.; Heverhagen, J.T.; et al. Conjugates Containing Two and Three Trithiolato-Bridged Dinuclear Ruthenium(II)-Arene Units as In Vitro Antiparasitic and Anticancer Agents. *Pharmaceuticals* **2020**, *13*, 471. [CrossRef]
25. Ahmad, M.S.; Khalid, M.; Khan, M.S.; Shahid, M.; Ahmad, M.; Saeed, H.; Owais, M.; Ashafaq, M. Tuning Biological Activity in Dinuclear Cu(II) Complexes Derived from Pyrazine Ligands: Structure, Magnetism, Catecholase, Antimicrobial, Antibiofilm, and Antibreast Cancer Activity. *Appl. Organomet. Chem.* **2021**, *35*, 6221. [CrossRef]
26. Iqbal, M.; Ali, S.; Tahir, M.N.; Shah, N.A. Dihydroxo-Bridged Dimeric Cu(II) System Containing Sandwiched Non-Coordinating Phenylacetate Anion: Crystal Structure, Spectroscopic, Antibacterial, Antifungal, and DNA-Binding Studies of [(Phen)(H_2O)Cu(OH)$_2$Cu(H_2O)(Phen)]2L·6H_2O (HL = Phenylacetic Acid; Phen = 1,10-Phenanthroline). *J. Mol. Struct.* **2017**, *1143*, 23.
27. Swiątkowski, M.; Lanka, S.; Czylkowska, A.; Gas, K.; Sawicki, M. Structural, Spectroscopic, Thermal, and Magnetic Properties of a New Dinuclear Copper Coordination Compound with Tiglic Acid. *Materials* **2021**, *14*, 2148. [CrossRef] [PubMed]
28. Banerjee, A.; Das, D.; Ray, P.P.; Banerjee, S.; Chattopadhyay, S. Phenoxo-Bridged Dinuclear Mixed Valence Cobalt(III/II) Complexes with Reduced Schiff Base Ligands: Synthesis, Characterization, Band Gap Measurements, and Fabrication of Schottky Barrier Diodes. *Dalton Trans.* **2021**, *50*, 1721. [CrossRef]
29. Borkar, A.; Nnabuike, G.G.; Obaleye, J.A.; Harihar, S.; Patil, A.S.; Butcher, R.J.; Salunke-Gawali, S. Manganese(II)-Imidazole Complexes of the Non-Steroidal Anti-Inflammatory Drug Mefenamic Acid: Synthesis and Structural Studies. *Inorg. Chim. Acta* **2020**, *512*, 119878. [CrossRef]

30. Sertcelik, M.; Ozbek, F.E.O.; Taslimi, P.; Necefoglu, H.; Hokelek, T. Supramolecular Complexes of Ni(II) and Co(II) 4-Aminobenzoate with 3-Cyanopyridine: Synthesis, Spectroscopic Characterization, Crystal Structure, and Enzyme Inhibitory Properties. *Appl. Organomet. Chem.* **2021**, *35*, 6182. [CrossRef]
31. Kowol, C.R.; Trondl, R.; Arion, V.B.; Jakupec, M.A.; Lichtscheidl, I.; Keppler, B.K. Fluorescence Properties and Cellular Distribution of the Investigational Anticancer Drug Triapine (3-Aminopyridine-2-Carboxaldehyde Thiosemicarbazone) and Its Zinc(II) Complex. *Dalton Trans.* **2010**, *39*, 704. [CrossRef]
32. Kahrovic, E.; Zahirović, A.; Pavelic, S.K.; Turkusic, E.; Harej, A. In Vitro Anticancer Activity of Binuclear Ru(II) Complexes with Schiff Bases Derived from 5-Substituted Salicylaldehyde and 2-Aminopyridine with Notably Low IC50 Values. *J. Coord. Chem.* **2017**, *70*, 1683. [CrossRef]
33. Soliman, S.M.; Elsilk, S. Synthesis, Structural Analyses, and Antimicrobial Activity of the Water-Soluble 1D Coordination Polymer [Ag(3-Aminopyridine)]ClO_4. *J. Mol. Struct.* **2017**, *1149*, 58. [CrossRef]
34. Suksrichavalit, T.; Prachayasittikul, S.; Nantasenamat, C.; Isarankura-Na-Ayudhya, C.; Prachayasittikul, V. Copper Complexes of Pyridine Derivatives with Superoxide Scavenging and Antimicrobial Activities. *Eur. J. Med. Chem.* **2009**, *44*, 3259. [CrossRef]
35. Machura, B.; Jaworska, M.; Kruszynski, R. Synthesis, Crystal, Molecular and Electronic Structure of the [$ReBr_3$(NO)($AsPh_3$)(pzH)] Complex. *Polyhedron* **2004**, *23*, 2523. [CrossRef]
36. Sun, Y.J.; Zhao, B.; Cheng, P. Synthesis and Characterization of Unusual Heterotrinuclear Co(III)Ni(II)Co(III)Hydrotris(3,5-Dimethylpyrazolyl)Borate Complex with Mixed 1,1-Azide and Pyrazolate Bridges. *Inorg. Chem. Commun.* **2007**, *10*, 583. [CrossRef]
37. Pettinari, C.; Tabacaru, A.; Galli, S. Coordination Polymers and Metal–Organic Frameworks Based on Poly(pyrazole)-Containing Ligands. *Coord. Chem. Rev.* **2016**, *307*, 1. [CrossRef]
38. Mondal, G.; Jana, H.; Acharjya, M.; Santra, A.; Bera, P.; Jana, A.; Panja, A.; Bera, P. Synthesis, In Vitro Evaluation of Antibacterial, Antifungal, and Larvicidal Activities of Pyrazole/Pyridine-Based Compounds and Their Nanocrystalline MS (M = Cu and Cd) Derivatives. *Med. Chem. Res.* **2017**, *26*, 3046. [CrossRef]
39. Ajo, D.; Bencini, A.; Mani, F. Anisotropic Exchange in Dinuclear Complexes with Polyatomic Bridges. 2. Crystal and Molecular Structure and EPR Spectra of Tetraphenylphosphonium Bis(μ-pyrazolato)bisdihydrobis(1-pyrazolyl)boratodicuprate(II). Magneto-Structural Correlations in Bis(μ-pyrazolato)-Bridged Copper(II) Complexes. *Inorg. Chem.* **1988**, *27*, 2437.
40. Mahmoud, W.H.; Deghadi, R.G.; Mohamed, G.G. Novel Schiff Base Ligand and Its Metal Complexes with Some Transition Elements: Synthesis, Spectroscopic, Thermal Analysis, Antimicrobial and In Vitro Anticancer Activity. *Appl. Organomet. Chem.* **2016**, *30*, 221. [CrossRef]
41. Chakraborty, S.; Rajput, L.D.; Desiraju, G.R. Designing Ternary Co-Crystals with Stacking Interactions and Weak Hydrogen Bonds: 4,4′-Bis-Hydroxyazobenzene. *Cryst. Growth Des.* **2014**, *14*, 2571. [CrossRef]
42. Kong, Y.J.; Han, L.J. Synthesis, X-ray Structure Analysis, and Spectroscopic Characterization of trans-Aquabis(μ-benzoato-κ^2O′)Bis[μ-N,N′-Bis(4-methoxyphenyl)formamidinato-κ^2N′] Dimolybdenum(II). *J. Chem. Crystallogr.* **2017**, *47*, 208. [CrossRef]
43. Moro, A.C.; Watanabe, F.W.; Ananias, S.R.; Mauro, A.E.; Netto, A.V.G.; Lima, A.P.R.; Ferreira, J.G.; Santos, R.H.A. Supramolecular Assemblies of cis-Palladium Complexes Dominated by C-H···Cl Interactions. *Inorg. Chem. Commun.* **2006**, *9*, 493. [CrossRef]
44. Gogoi, A.; Dutta, D.; Verma, A.K.; Nath, H.; Frontera, A.; Guha, A.K.; Bhattacharyya, M.K. Energetically Favorable Anti-Electrostatic Hydrogen-Bonded Cationic Clusters in Ni(II) 3,5-Dimethylpyrazole Complexes: Anticancer Evaluation and Theoretical Studies. *Polyhedron* **2019**, *168*, 113. [CrossRef]
45. Eom, G.H.; Park, H.M.; Hyun, M.Y.; Jang, S.P.; Kim, C.; Lee, J.H.; Lee, S.J.; Kim, S.J.; Kim, Y. Anion Effects on the Crystal Structures of Zn^{II} Complexes Containing 2,2′-Bipyridine: Their Photoluminescence and Catalytic Activities. *Polyhedron* **2011**, *30*, 1555. [CrossRef]
46. Gogoi, A.; Islam, S.M.N.; Frontera, A.; Bhattacharyya, M.K. Supramolecular Association in Cu(II) and Co(II) Coordination Complexes of 3,5-Dimethylpyrazole: Experimental and Theoretical Studies. *Inorg. Chim. Acta* **2019**, *484*, 133. [CrossRef]
47. Dutta, D.; Chetry, S.; Gogoi, A.; Choudhury, B.; Guha, A.K.; Bhattacharyya, M.K. Supramolecular Association Involving Anion–π Interactions in Cu(II) Coordination Solids: Experimental and Theoretical Studies. *Polyhedron* **2018**, *151*, 381. [CrossRef]
48. Sharma, P.; Gogoi, A.; Verma, A.K.; Frontera, A.; Bhattacharyya, M.K. Charge-Assisted Hydrogen Bond and Nitrile···Nitrile Interaction Directed Supramolecular Associations in Cu(II) and Mn(II) Coordination Complexes: Anticancer, Hematotoxicity, and Theoretical Studies. *New J. Chem.* **2020**, *44*, 5473. [CrossRef]
49. Harit, T.; Malek, F.; El-Bali, B.; Khan, A.; Dalvandi, K.; Marasini, B.P.; Noreen, S.; Malik, R.; Khan, S.; Choudhary, M.I. Synthesis and Enzyme Inhibitory Activities of Some New Pyrazole-Based Heterocyclic Compounds. *Med. Chem. Res.* **2012**, *21*, 2772. [CrossRef]
50. Lunagariya, M.V.; Thakor, K.P.; Varma, R.R.; Waghela, B.N.; Pathak, C.; Patel, M.N. Synthesis, Characterization, and Biological Application of 5-Quinoline 1,3,5-Trisubstituted Pyrazole-Based Platinum(II) Complexes. *MedChemComm* **2018**, *9*, 282. [CrossRef] [PubMed]

51. Karrouchi, K.; Yousfi, E.B.; Sebbar, N.K.; Ramli, Y.; Taoufik, J.; Ouzidan, Y.; Ansar, M.; Mabkhot, Y.N.; Ghabbour, H.A.; Radi, S. New Pyrazole-Hydrazone Derivatives: X-ray Analysis, Molecular Structure Investigation via Density Functional Theory (DFT), and Their High In-Situ Catecholase Activity. *Int. J. Mol. Sci.* **2017**, *18*, 2215. [CrossRef] [PubMed]
52. Mirdya, S.; Roy, S.; Chatterjee, S.; Bauza, A.; Frontera, A.; Chattopadhyay, S. Importance of π-Interactions Involving Chelate Rings in Addition to Tetrel Bonds in Crystal Engineering: A Combined Experimental and Theoretical Study on a Series of Hemi- and Holodirected Nickel(II)/Lead(II) Complexes. *Cryst. Growth Des.* **2019**, *19*, 5869. [CrossRef]
53. Mahmudov, K.T.; Kopylovich, M.N.; Silva, M.F.C.G.; Pombeiro, A.J.L. Non-Covalent Interactions in the Synthesis of Coordination Compounds: Recent Advances. *Coord. Chem. Rev.* **2017**, *345*, 54. [CrossRef]
54. Dutta, D.; Sharma, P.; Gomila, R.M.; Frontera, A.; Barcelo-Oliver, M.; Verma, A.K.; Baishya, T.; Bhattacharyyaa, M.K. Supramolecular Assemblies Involving Unconventional Non-Covalent Contacts in Pyrazole-Based Coordination Compounds of Co(II) and Cu(II) Pyridinedicarboxylates: Antiproliferative Evaluation and Theoretical Studies. *Polyhedron* **2022**, *224*, 116025. [CrossRef]
55. El-ghamry, M.A.; Shebl, M.; Saleh, A.A.; Khalil, S.M.E.; Amir, M.D.; Ali, A.M. Spectroscopic Characterization of Cu(II), Ni(II), Co(II) Complexes, and Nano Copper Complex Bearing a New S, O, N-Donor Chelating Ligand. 3D Modeling Studies, Antimicrobial, Antitumor, and Catalytic Activities. *J. Mol. Struct.* **2022**, *1249*, 131587. [CrossRef]
56. Fabiyi, F.S.; Olanrewaju, A.A. Synthesis, Characterization, Thermogravimetric and Antioxidant Studies of New Cu(II), Fe(II), Mn(II), Cu(II), Zn(II), Co(II), and Ni(II) Complexes with Benzoic Acid and 4,4,4-Trifluoro-1-(2-Naphthyl)-1,3-Butanedione. *Int. J. Chem.* **2019**, *11*, 1. [CrossRef]
57. Rossin, A.; Credico, B.D.; Giambastiani, G.; Peruzzini, M.; Pescitelli, G.; Reginato, G.; Borfecchia, E.; Gianolio, D.; Lamberti, C.; Bordiga, S. Synthesis, Characterization, and CO2 Uptake of a Chiral Co(II) Metal–Organic Framework Containing a Thiazolidine-Based Spacer. *J. Mater. Chem.* **2012**, *22*, 10335. [CrossRef]
58. Etter, M.C. Encoding and Decoding Hydrogen-Bond Patterns of Organic Compounds. *Acc. Chem. Res.* **1990**, *23*, 120. [CrossRef]
59. Janiak, C. A Critical Account on π–π Stacking in Metal Complexes with Aromatic Nitrogen-Containing Ligands. *J. Chem. Soc., Dalton Trans.* **2000**, *21*, 3885. [CrossRef]
60. He, X.; Li, Y.; Li, G.; Li, Y.; Zhang, P.; Xu, J.; Wang, Y. Synthesis, Crystal Structure, and Magnetic Properties of a New 1D Cobalt(II) Complex with 1,10-Phenanthroline and 3,5-Dinitrosalicylate Acid Ligands. *Inorg. Chem. Commun.* **2005**, *8*, 983. [CrossRef]
61. Ali, H.A.; Shamma, A.A.; Kamel, S. New Mixed Ligand Cobalt (II/III) Complexes Based on the Drug Sodium Valproate and Bioactive Nitrogen-Donor Ligands: Synthesis, Structure and Biological Properties. *J. Mol. Struct.* **2017**, *1142*, 40. [CrossRef]
62. Dojer, B.; Pevec, A.; Jagodic, M.; Kristl, M.; Drofenik, M. Three New Cobalt(II) Carboxylates with 2-, 3-, and 4-Aminopyridine: Syntheses, Structures, and Magnetic Properties. *Inorg. Chim. Acta* **2012**, *383*, 98. [CrossRef]
63. Dojer, B.; Pevec, A.; Šegedin, P.; Jagličić, Z.; Stropnik, Č.; Kristl, M.; Drofenik, M. Cobalt (II) Coordination Compounds with Acetate and 2-Aminopyridine Ligands: Synthesis, Characterization, Structures and Magnetic Properties of Two Polymorphic Forms. *Inorg. Chim. Acta* **2010**, *363*, 1343. [CrossRef]
64. Muthukkumar, M.; Karthikeyan, A.; Kamalesu, S.; Kadri, M.; Jennifer, S.J.; Razak, I.A.; Nehru, S. Synthesis, Crystal Structure, Optical and DFT Studies of a Novel Co(II) Complex with the Mixed Ligands 3-Bromothiophene-2-Carboxylate and 2-Aminopyridine. *J. Mol. Struct.* **2022**, *1270*, 133953. [CrossRef]
65. Zhong, D.-C.; Guo, G.-Q.; Zuo, X.-H.; Deng, J.-H.; Yuan, L.; Zhu, R.-H. Bis(2-Aminopyridine-κN1) Bis(Benzoato-κO) Cobalt(II). *Acta Crystallogr. Sect. E Struct. Rep. Online* **2008**, *64*, m88. [CrossRef]
66. Swiatkowski, M.; Sieranski, T.; Bogdan, M.; Kruszynski, R. Structural Insights into Influence of Isomerism on Properties of Open Shell Cobalt Coordination System. *Molecules* **2019**, *24*, 3357. [CrossRef] [PubMed]
67. Boro, M.; Banik, S.; Gomila, R.M.; Frontera, A.; Barcelo-Oliver, M.; Bhattacharyya, M.K. Supramolecular Assemblies in Mn(II) and Zn(II) Metal–Organic Compounds Involving Phenanthroline and Benzoate: Experimental and Theoretical Studies. *Inorganics* **2024**, *12*, 139. [CrossRef]
68. Mahapatra, T.S.; Bauza, A.; Dutta, D.; Mishra, S.; Frontera, A.; Ray, D. Carboxylate Coordination Assisted Aggregation for Quasi-Tetrahedral and Partial-Dicubane [Cu4] Coordination Clusters. *ChemistrySelect* **2016**, *1*, 64. [CrossRef]
69. Orhan, O.; Colak, A.T.; Emen, F.M.; Kismali, G.; Meral, O.; Sel, T.; Cilgi, G.K.; Tas, M. Syntheses of Crystal Structures and In Vitro Cytotoxic Activities of New Copper(II) Complexes of Pyridine-2,6-Dicarboxylate. *J. Coord. Chem.* **2015**, *68*, 4003. [CrossRef]
70. Manna, S.C.; Mistria, S.; Jana, A.D. A Rare Supramolecular Assembly Involving Ion Pairs of Coordination Complexes with a Host–Guest Relationship: Synthesis, Crystal Structure, Photoluminescence, and Thermal Study. *CrystEngComm* **2012**, *14*, 7415. [CrossRef]
71. Bhattacharyya, M.K.; Dutta, D.; Islam, S.M.N.; Frontera, A.; Sharma, P.; Verma, A.K.; Das, A. Energetically Significant Antiparallel π-Stacking Contacts in Co(II), Ni(II), and Cu(II) Coordination Compounds of Pyridine-2,6-Dicarboxylates: Antiproliferative Evaluation and Theoretical Studies. *Inorg. Chim. Acta* **2020**, *501*, 119233. [CrossRef]
72. Aycan, T. Synthesis, Crystal Structure, Spectroscopic (FT-IR, UV–Vis, EPR) and Hirshfeld Surface Analysis Studies of Zn(II)-Benzoate Coordination Dimer. *J. Mol. Struct.* **2021**, *1223*, 128943. [CrossRef]

73. Nakamoto, K. *Infrared and Raman Spectra of Inorganic and Coordination Compounds*, 5th ed.; John Wiley & Sons: New York, NY, USA, 1997.
74. Sharma, P.; Dutta, D.; Gomila, R.M.; Frontera, A.; Barcelo-Oliver, M.; Verma, A.K.; Bhattacharyya, M.K. Benzoato Bridged Dinuclear Mn(II) and Cu(II) Compounds Involving Guest Chlorobenzoates and Dimeric Paddle Wheel Supramolecular Assemblies: Antiproliferative Evaluation and Theoretical Studies. *Polyhedron* **2021**, *208*, 115409. [CrossRef]
75. Dutta, D.; Islam, S.M.N.; Saha, U.; Chetry, S.; Guha, A.K.; Bhattacharyya, M.K. Cu(II) and Co(II) Coordination Solids Involving Unconventional Parallel Nitrile(π)–Nitrile(π) and Energetically Significant Cooperative Hydrogen Bonding Interactions: Experimental and Theoretical Studies. *J. Mol. Struct.* **2019**, *1195*, 733. [CrossRef]
76. Dutta, D.; Islam, S.M.N.; Saha, U.; Chetry, S.; Guha, A.K.; Bhattacharyya, M.K. Structural Topology of Weak Non-Covalent Interactions in a Layered Supramolecular Coordination Solid of Zinc Involving 3-Aminopyridine and Benzoate: Experimental and Theoretical Studies. *J. Chem. Crystallogr.* **2018**, *48*, 156. [CrossRef]
77. Akyüz, S. The FT-IR Spectra of Transition Metal 3-Aminopyridine Tetracyanonickelate Complexes. *J. Mol. Struct.* **1998**, *449*, 23. [CrossRef]
78. Bora, S.J.; Das, B.K. Synthesis and Properties of a Few 1-D Cobaltous Fumarates. *J. Solid State Chem.* **2012**, *192*, 93. [CrossRef]
79. Batool, S.S.; Gilani, S.R.; Tahir, M.N.; Harrison, W.T.A.Z. Syntheses and Structures of Monomeric and Dimeric Ternary Complexes of Copper(II) with 2,2′-Bipyridyl and Carboxylate Ligands. *Z. Anorg. Allg. Chem.* **2016**, *642*, 1364. [CrossRef]
80. Basumatary, D.; Lal, R.A.; Kumar, A. Synthesis and Characterization of Low- and High-Spin Manganese(II) Complexes of Polyfunctional Adipoyldihydrazone: Effect of Coordination of N-Donor Ligands on Stereo-Redox Chemistry. *J. Mol. Struct.* **2015**, *1092*, 122. [CrossRef]
81. Islam, S.M.N.; Dutta, D.; Guha, A.K.; Bhattacharyya, M.K. An Unusual Werner-Type Clathrate of Mn(II) Benzoate Involving Energetically Significant Weak C–H$\cdots$C Contacts: A Combined Experimental and Theoretical Study. *J. Mol. Struct.* **2019**, *1175*, 130. [CrossRef]
82. Goher, M.A.; Hafez, A.K.; Abu-Youssef, M.A.M.; Badr, A.M.A.; Gspan, C.; Mautner, F.A. New Metal(II) Complexes Containing Monodentate and Bridging 3-Aminopyridine and Azido Ligands. *Polyhedron* **2004**, *23*, 2349. [CrossRef]
83. Wang, R.; Wang, S.; Shi, S.; Zang, J. Crystal Structure and Properties of a Terbium *m*-Methylbenzoate Complex with 1,10-Phenanthroline. *J. Coord. Chem.* **2002**, *55*, 215. [CrossRef]
84. Piccinini, F.; Tesei, A.; Arienti, C.; Bevilacqua, A. Cell Counting and Viability Assessment of 2D and 3D Cell Cultures: Expected Reliability of the Trypan Blue Assay. *Biol. Proced. Online* **2017**, *19*, 1. [CrossRef] [PubMed]
85. Lebeau, P.F.; Chen, J.; Byun, J.H.; Platko, K.; Austin, R.C. The Trypan Blue Cellular Debris Assay: A Novel Low-Cost Method for the Rapid Quantification of Cell Death. *MethodsX* **2019**, *6*, 1174. [CrossRef] [PubMed]
86. Bianchi, M.E.; Manfredi, A. Chromatin and Cell Death. *Biochim. Biophys. Acta Gene Struct. Expr.* **2004**, *1677*, 181. [CrossRef]
87. Wyllie, A.H.; Beattie, G.J.; Hargreaves, A.D. Chromatin Changes in Apoptosis. *Histochem. J.* **1981**, *13*, 681. [CrossRef]
88. Verma, A.K.; Prasad, S.B. Antitumor Effect of Blister Beetles: An Ethno-Medicinal Practice in Karbi Community and Its Experimental Evaluation Against a Murine Malignant Tumor Model. *J. Ethnopharmacol.* **2013**, *148*, 869. [CrossRef] [PubMed]
89. Gogoi, A.; Das, A.; Frontera, A.; Verma, A.K.; Bhattacharyya, M.K. Energetically Significant Unconventional π–π Contacts Involving Fumarate in a Novel Coordination Polymer of Zn(II): In-Vitro Anticancer Evaluation and Theoretical Studies. *Inorg. Chim. Acta* **2019**, *493*, 1. [CrossRef]
90. Tanida, S.; Mizoshita, T.; Ozeki, K.; Tsukamoto, H.; Kamiya, T.; Kataoka, H.; Joh, T. Mechanisms of Cisplatin-Induced Apoptosis and of Cisplatin Sensitivity: Potential of BIN1 to Act as a Potent Predictor of Cisplatin Sensitivity in Gastric Cancer Treatment. *Int. J. Surg. Oncol.* **2012**, *2012*, 862879. [CrossRef]
91. Lima, A.P.; Pereira, F.C.; Almeida, M.A.P.; Mello, F.M.S.; Pires, W.C.; Pinto, T.M.; Delella, F.K.; Felisbino, S.L.; Moreno, V.; Batista, A.A.; et al. Cytoxicity and Apoptotic Mechanism of Ruthenium(II) Amino Acid Complexes in Sarcoma-180 Tumor Cells. *PLoS ONE* **2014**, *9*, 105865. [CrossRef]
92. Saha, S.K.; Lee, S.B.; Won, J.; Choi, H.Y.; Kim, K.; Yang, G.M.; Cho, S.G. Correlation Between Oxidative Stress, Nutrition, and Cancer Initiation. *Int. J. Mol. Sci.* **2017**, *18*, 1544. [CrossRef]
93. Verma, A.K.; Kumar, V.; Singh, S.; Goswami, B.C.; Camps, I.; Sekar, A.; Yoon, S.; Lee, S. Repurposing Potential of Ayurvedic Medicinal Plants Derived Active Principles Against SARS-CoV-2 Associated Target Proteins Revealed by Molecular Docking, Molecular Dynamics, and MM-PBSA Studies. *Biomed. Pharmacother.* **2021**, *137*, 1.
94. Thomsen, R.; Christensen, M.H. MolDock: A New Technique for High Accuracy Molecular Docking. *J. Med. Chem.* **2006**, *49*, 3315. [CrossRef]
95. Verma, A.K.; Aggarwal, R. Repurposing Potential of FDA-Approved and Investigational Drugs for COVID-19 Targeting SARS-CoV-2 Spike and Main Protease and Validation by Machine Learning Algorithm. *Chem. Biol. Drug Des.* **2020**, *97*, 836. [CrossRef] [PubMed]
96. Ashkenazi, A.; Fairbrother, W.J.; Leverson, J.D.; Souers, A.J. From Basic Apoptosis Discoveries to Advanced Selective BCL-2 Family Inhibitors. *Nat. Rev. Drug Discov.* **2017**, *16*, 273. [CrossRef] [PubMed]

97. *SADABS*, V2.05; Bruker AXS: Madison, WI, USA, 1999.
98. Sheldrick, G.M. A Short History of SHELX. *Acta Crystallogr.* **2008**, *64*, 112. [CrossRef] [PubMed]
99. Dolomanov, O.V.; Bourhis, L.J.; Gildea, R.J.; Howard, J.A.; Puschmann, H. OLEX2: A Complete Structure Solution, Refinement and Analysis Program. *J. Appl. Crystallogr.* **2009**, *42*, 339. [CrossRef]
100. Brandenburg, K. *Diamond*, 3.1f; Crystal Impact GbR: Bonn, Germany, 2008.
101. Ahlrichs, R.; Bär, M.; Hacer, M.; Horn, H.; Kömel, C. Electronic Structure Calculations on Workstation Computers: The Program System Turbomole. *Chem. Phys. Lett.* **1989**, *162*, 165. [CrossRef]
102. Becke, A.D. Density-Functional Exchange-Energy Approximation with Correct Asymptotic Behavior. *Phys. Rev. A* **1988**, *38*, 3098. [CrossRef]
103. Caldeweyher, E.; Mewes, J.-M.; Ehlert, S.; Grimme, S. Extension and Evaluation of the D4 London-Dispersion Model for Periodic Systems. *Phys. Chem. Chem. Phys.* **2020**, *22*, 8499. [CrossRef]
104. Weigend, F. Accurate Coulomb-Fitting Basis Sets for H to Rn. *Phys. Chem. Chem. Phys.* **2006**, *8*, 1057. [CrossRef] [PubMed]
105. Bader, R.F.W. A Quantum Theory of Molecular Structure and Its Applications. *Chem. Rev.* **1991**, *91*, 893. [CrossRef]
106. Johnson, E.R.; Keinan, S.; Mori-Sánchez, P.; Contreras-García, J.; Cohen, A.J.; Yang, W. Revealing Noncovalent Interactions. *J. Am. Chem. Soc.* **2010**, *132*, 6498. [CrossRef] [PubMed]
107. Lu, T.; Chen, F. Multiwfn: A Multifunctional Wavefunction Analyzer. *J. Comput. Chem.* **2012**, *33*, 580. [CrossRef]
108. Humphrey, J.W.; Dalke, A.; Schulten, K. VMD: Visual Molecular Dynamics. *J. Mol. Graphics* **1996**, *14*, 33. [CrossRef]
109. Dutta, D.; Singh, N.S.; Aggarwal, R.; Verma, A.K. *Cordyceps militaris*: A Comprehensive Study on Laboratory Cultivation and Anticancer Potential in Dalton's Ascites Lymphoma Tumor Model. *Anti-Cancer Agents Med. Chem.* **2024**, *24*, 668. [CrossRef]
110. Strober, W. Trypan Blue Exclusion Test of Cell Viability. *Curr. Protoc. Immunol.* **2015**, *111*, A3-B. [CrossRef] [PubMed]
111. Das, J.; Fatmi, M.Q.; Devi, M.; Singh, N.S.; Verma, A.K. Antitumor Activity of Cordycepin in Murine Malignant Tumor Cell Line: An In Vitro and In Silico Study. *J. Mol. Struct.* **2023**, *1297*, 136946. [CrossRef]
112. Verma, A.K.; Prasad, S.B. Bioactive Component, Cantharidin from *Mylabris cichorii* and Its Antitumor Activity Against Ehrlich Ascites Carcinoma. *Cell Biol. Toxicol.* **2012**, *28*, 133. [CrossRef] [PubMed]

Disclaimer/Publisher's Note: The statements, opinions and data contained in all publications are solely those of the individual author(s) and contributor(s) and not of MDPI and/or the editor(s). MDPI and/or the editor(s) disclaim responsibility for any injury to people or property resulting from any ideas, methods, instructions or products referred to in the content.